

Benchmarking GOCART-2G in the Goddard Earth Observing System (GEOS)

Allison B. Collow^{1,2}, Peter R. Colarco³, Arlindo M. da Silva², Virginie Buchard^{1,2}, Huisheng Bian^{1,3}, Mian Chin³, Sampa Das^{3,4}, Ravi Govindaraju^{2,5}, Dongchul Kim^{1,3}, and Valentina Aquila⁶

5 ¹University of Maryland Baltimore County, Baltimore, Maryland, US

²Global Modeling and Assimilation Office, NASA Goddard Space Flight Center, Greenbelt, Maryland, US

³Atmospheric Chemistry and Dynamics Lab, NASA Goddard Space Flight Center, Greenbelt, Maryland, US

⁴University of Maryland, College Park, MD

⁵Science Systems and Applications, Inc., Lanham, Maryland, US

10 ⁶American University, Department of Environmental Science, Washington, District of Columbia, US

Correspondence to: Allison Collow (allison.collow@nasa.gov)

Abstract. The Goddard Chemistry Aerosol Radiation and Transport (GOCART) model, which controls the sources, sinks, and chemistry of aerosols within the Goddard Earth Observing System (GEOS), recently underwent a major refactoring and update to the representation of physical processes. ~~This paper serves to document code changes that were included in GOCART 2nd Generation (GOCART-2G) and establishes a benchmark simulation that is to be used for future development of the system. The code refactoring increases flexibility such multiple instances of an aerosol species can be run and interact with radiation and cloud microphysics, in addition to the output of multiple wavelength aerosol optical properties in support of data assimilation. From a science perspective, a new radiatively active tracer, brown carbon, was added to distinguish smoke from other sources of organic aerosol thereby improving optical properties entering the radiative calculations.~~ A four-year benchmark simulation utilizing the new version of the model code, termed GOCART 2nd Generation (GOCART-2G) and coupled to the Goddard Earth Observing System (GEOS) model, was evaluated using in situ and space borne measurements to develop a baseline and prioritize future development. A comparison of simulated aerosol optical depth between GOCART-2G and MODIS retrievals indicates the model captures the overall spatial pattern and seasonal cycle of aerosol optical depth but overestimates aerosol extinction over dusty regions and underestimates aerosol extinction over northern hemisphere boreal forests, requiring further tuning of emissions. This MODIS-based analysis is corroborated by comparisons to MISR and selected AERONET stations, however discrepancies between the Aqua and Terra satellites indicate there is a diurnal component to biases in aerosol optical depth over South Asia and Northern Africa. Despite the underestimate of aerosol optical depth in biomass burning regions in GEOS, there is an overestimate in the surface mass of organic carbon in the United States, especially during the summer months. Over Europe, GOCART-2G is unable to match the summertime peak in aerosol optical depth, opposing the observed late-fall and early-spring peaks in surface mass concentration. A comparison of the vertical profile of attenuated backscatter to observations from CALIPSO indicates the GEOS model-a is capable of capturing the vertical profile of aerosol however the mid-troposphere plumes of dust in the North Atlantic and smoke in the Southeast

35 [Atlantic are perhaps too low in altitude. The results presented highlight priorities for future development with GOCART-2G, including improvements for dust, biomass burning aerosols, and anthropogenic aerosols.](#)

1 Introduction

Aerosols are an important component of the atmosphere, with implications for air quality, cloud lifecycle, and the radiation budget. As general circulation models strive to take a comprehensive Earth-system approach, aerosol modules have become coupled to the atmosphere for use in numerical weather prediction (Colarco et al., 2010; Rémy et al., 2019), seasonal prediction (Molod et al., 2020), and reanalyses (Buchard et al., 2017; Randles et al., 2017), and have been shown to increase forecast skill through changes in temperature (Bozzo et al., 2020). Aerosol modules handle the sources, sinks, and chemistry within models; however, they ~~vary-differ~~ in complexity—~~for example, representing particle size distribution and mixing state variously in terms of bulk quantities or discretized in sections or modes~~—and their diverse assumptions result in uncertainty and diversity in the simulated aerosol life cycle and optical properties (Textor et al., 2006; Tsigaridis et al., 2014; Gliß et al., 2021).

A commonly used bulk aerosol module is the Goddard Chemistry Aerosol Radiation and Transport (GOCART) module, which traces its origin to an offline aerosol transport model driven by the assimilated meteorological fields from the Goddard Earth Observing System (GEOS; Chin et al. 2002, 2014). GOCART was later coupled to GEOS to enable short-term aerosol forecasts and provide a platform for aerosol data assimilation (Colarco et al., 2010). It has also been implemented in NOAA’s Unified Forecast System (Lu et al., 2016, Zhang et al., 2022) and the Weather Research and Forecasting Model (WRF). In its legacy form, GOCART has handled the ~~sources, sinks, and chemistry of externally mixed aerosols~~ aerosols within the GEOS model and its individual systems. Near real-time aerosol forecasts began in ~~the GEOS-Forward Processing (FP) configuration of GEOS (GEOS FP)~~ in 2011 (Figure S1), though GOCART had previously been used within GEOS for field campaign support. An aerosol analysis has been produced retrospectively in reanalysis systems such as the Modern Era retrospective Analysis for Research and Applications, Version 2 (MERRA-2, Randles et al. 2017, Buchard et al. 2017), and GOCART is included in the subseasonal to season forecast system, GEOS S2S (Molod et al., 2020).

~~This paper serves to outline updates that have been implemented in GOCART since the production of MERRA-2, including a suite of science changes and code improvements that encompass GOCART second generation (GOCART-2G). GOCART-2G is intended to be used in future versions of GEOS numerical weather prediction, subseasonal to seasonal prediction, and reanalysis products. Although GEOS is a modular system that can be run with other aerosol modules for research purposes (e.g., Case et al., 2023), sectional and modal schemes are too computationally expensive to be used in a near real time, operational environment. Therefore, proper documentation and evaluation for GOCART-2G is a necessity.~~

Embedded within the GEOS model, GOCART has participated in aerosol model intercomparison studies associated with AeroCom and is included in the International Cooperative for Aerosol Prediction (ICAP) multi-model ensemble (MME) (Xian et al., 2019). Notable features of the module have been documented in the literature as a result. The all-sky aerosol optical

depth (AOD) in GEOS-GOCART is very close to the median for the models that participated in AeroCom Phase III, however there is variability among the aerosol species (Gliß et al, 2021). The optical depth and mass burden for nitrate and dust in GEOS-GOCART is above the AeroCom Phase III model median. Focusing on African dust, Kim et al. (2014) showed that GOCART had over double the dust emissions from all other models investigated, leading to an overestimate of AOD over northern Africa yet and underestimated AOD in the transport region of the North Atlantic. Yu et al. (2020) noted that GEOS underestimated emissions of dust from haboobs and did not loft dust high enough into the middle troposphere for sufficient transport, resulting in an underestimate of the dust AOD in the Caribbean during a substantial dust event in June 2020. It was also pointed out by Kramer et al. (2020) that transported dust is overabundant in the boundary layer and has a particle size that is too large. Corroborated with respect to observations by Collow et al. (2022), Burgos demonstrated that GEOS-GOCART has an excessive hygroscopic growth rate for carbonaceous aerosol and a smaller variability for $f(\text{RH})$ relative to the other participating models. This indicates that even if the mass burden is the same, the optical depth could be very different from other models, and vice versa.

This paper serves to outline updates that have been implemented in GOCART since the production of MERRA-2, including a suite of science changes and code improvements that encompass GOCART second generation (GOCART-2G). GOCART-2G is intended to be used in future versions of GEOS numerical weather prediction, subseasonal to seasonal prediction, and reanalysis products. While sectional and modal aerosol schemes have been implemented in GEOS since the development of GOCART (e.g., Case et al., 2023), they are too computationally expensive to be used in a near-real time, operational environment. Therefore, GOCART-2G will continue to be used in the GEOS system, and so proper documentation and evaluation of it is a necessity.

Though GOCART has evolved over the past two decades, aAs described in Section 2, a recent overhaul of the GOCART module has been completed to pave the way for future development of the aerosol module. A four-year simulation is then evaluated in Section 4 to benchmark the performance of GOGART-2G and provide a reference for future development of aerosol modelling within GEOS. One major difference between the evaluation presented here compared to prior evaluations of aerosols within GEOS from the MERRA-2 system (Randles et al. (2017); Buchard et al. 2017) is that here, aerosol optical depth (AOD) is not assimilated, like Colarco et al. (2010). While meteorology is constrained in the benchmark simulation, no aerosol data assimilation is included, and aerosol distributions are governed solely by processes in the model.

Modelled aerosols are driven by emissions that are prescribed, as is the case for smoke and anthropogenic emissions, or calculated by parameterizations coupled with meteorological fields, such as for sea salt and dust. Choices for which dataset or parameterization to use can have a large impact on the modelled aerosol loading. For example, uncertainty arises for biomass burning, where six commonly used emission datasets were found to differ by a factor of 3.8 (Pan et al., 2020), and dust optical depth model diversity is dominated by the simulated dust source strength (Kim et al., 2019).

Aerosol modules also require assumptions regarding the number of aerosol species, size of aerosol particles, particle size dependent gravitational settling, and particle swelling in response to changes in relative humidity. Simpler aerosol bulk

aerosol models typically prescribe sizes and lack microphysical processes found in modal (eg. Liu et al., 2016) and sectional schemes (eg. Yu et al., 2015). Among the global models included in the International Cooperative for Aerosol Prediction (ICAP) multi-model ensemble (MME) study, there is variability in the species, particularly related to nitrate and biomass burning smoke, as well as the number of size bins used to discretize the particle size distribution for a given species (Table 1 of Xian et al., 2019). The settling for each size bin can follow the same size-based parameterization for each bin or settle at different rates depending on the size bin. While some aerosols are hydrophobic, others swell in the presence of water vapor, which can affect particle settling speeds and optical properties. A large range in the scattering enhancement factor as a function of relative humidity, $f(\text{RH})$, was found in a comparison of ten Earth system models (Burgos et al., 2020), which can result in varying aerosol extinction even where aerosol loadings are similar.

A commonly used bulk aerosol module is the Goddard Chemistry Aerosol Radiation and Transport (GOCART) module, which traces its origin to an offline aerosol transport model driven by the assimilated meteorological fields from the Goddard Earth Observing System (GEOS; Chin et al. 2002, 2014). GOCART was later coupled to GEOS to enable short term aerosol forecasts and provide a platform for aerosol data assimilation (Colareo et al., 2010). It has also been implemented in NOAA's Unified Forecast System (Lu et al., 2016, Zhang et al., 2022) and the Weather Research and Forecasting Model (WRF). In its legacy form, GOCART has handled the sources, sinks, and chemistry of externally mixed aerosols within the GEOS model and its individual systems. Near real-time aerosol forecasts began in GEOS Forward Processing in 2011 (Figure S1), though GOCART had previously been used within GEOS for field campaign support. An aerosol analysis has been produced retrospectively in reanalysis systems such as the Modern Era retrospective Analysis for Research and Applications, Version 2 (MERRA-2, Randles et al. 2017, Buchard et al. 2017). Though GOCART has evolved over the past two decades, a recent overhaul of the module has been completed to pave the way for future development.

This paper serves to document updates that have been implemented in GOCART since the production of MERRA-2, including a suite of science changes and code improvements that encompass GOCART second generation (GOCART-2G). A four-year simulation is then evaluated in Section 4 to benchmark the performance of GOCART-2G and provide a reference for future development of aerosol modelling within GEOS. One major difference between the evaluation presented here compared to prior evaluations of aerosols within GEOS from the MERRA-2 system (Randles et al. (2017); Buchard et al. 2017) is that here, aerosol optical depth (AOD) is not assimilated, like Colareo et al. (2010). While meteorology is constrained in the benchmark simulation, no aerosol data assimilation is included, and aerosol distributions are governed solely by processes in the model. GOCART-2G is intended to be used in future versions of GEOS FP and reanalysis products with GEOS, hence the need for proper documentation and evaluation.

2.1 Background

GOCART-2G includes seven radiatively active aerosol ~~tracers-species~~ that are considered externally mixed: sea salt, dust, organic carbon, brown carbon, black carbon, sulphate, and nitrate. Like in MERRA-2, sea salt (SS) and dust (DU) are comprised of five non-interacting size bins (Table A1). Sea salt emissions are based on Gong (2003), with some key modifications: 1) friction velocity is used instead of 10 m wind speed, which required tuning for the constants within the parameterization, and 2) addition of a correction term dependent on sea surface temperature, similar to the work of Jaegle et al. (2011) but tuned to improve the agreement of simulated sea salt AOD with MODIS retrieved AOD. ~~Default dD~~ Dust emissions follow Ginoux et al. (2001), see Table 1. The smallest size bin for dust is further divided into four sub-bins for optics calculations according to Tegen and Lacis (1996). Organic (OC), brown (BR), and black (BC) carbon have hydrophobic and hydrophilic components. Upon emission, 50% of organic carbon, 50% of brown carbon, and 80% of black carbon are considered hydrophobic (Chin et al., 2002) and transition to hydrophilic at a e-folding time scale of 2.5 days (Maria et al., 2004). A factor of 1.8 is implemented upon emission to convert organic carbon, including the tracer for brown carbon, to particulate organic matter (POM), which has been increased from the factor of 1.4 used in MERRA-2 based on observations from recent airborne campaigns (Hodzic et al., 2020). Emission sources of carbonaceous aerosol include biomass burning, biogenic, and anthropogenic emissions. Biomass burning emissions are released uniformly throughout the planetary boundary layer (PBL) depth, while anthropogenic emissions enter only in the lowest model level. While the source data for biomass burning emissions is consistent with MERRA-2 ([the Quick Fire Emissions Dataset; QFED, Darmenov and da Silva, 2015](#)), anthropogenic emissions now come from the Community Emissions Data System (CEDS) v_2021_04_21 (Table 1; Hoesly et al., 2018; doi: 10.5281/zenodo.4741285); currently CEDS emissions are available up to 2019. [The CEDS emissions dataset was chosen to be consistent with other modelling efforts including the Coupled Model Intercomparison Project Phase 6 \(CMIP6; Feng et al., 2020\) and the Chemistry-Climate Model Initiative.](#) Additional information is provided in [Section 2.2](#) [the supplemental document](#) pertaining to the implementation of brown carbon and secondary organic aerosol (SOA) as these tracers were added as part of GOCART-2G.

A single tracer is used for the sulphate ion, SO_4^{2-} . Volcanic emissions of SO_2 are from Carn et al. (2017) with explosive emissions updated through 2021 as of this writing, while biomass burning and anthropogenic emissions of SO_2 and SO_4^{2-} are consistent with the carbon emissions (Table 1). Sulphate chemistry follows Chin et al. (2000) in which sulphate is formed from the oxidation of SO_2 and the precursor dimethyl ~~sulfidesulphide~~ (DMS) in the presence of hydroxide (OH) and NO_3 and aqueously via titration of hydrogen peroxide (H_2O_2). In a traditional GOCART-2G simulation, these oxidant fields are provided in archived monthly data from previous full chemistry simulations and the diurnal cycle is imposed on the OH field. GOCART-2G can also run interactively with a gas chemistry module in which these oxidant fields are updated at every time step.

Nitrate was incorporated into GEOS in 2017, after production began for MERRA-2, based on the approach used for the Global Modeling Initiative (GMI) chemistry transport model (CTM) (Bian et al. 2017). Three particle size groups are

included for nitrate aerosol in GOCART-2G: a fine mode bin and two coarse mode bins (Table 1 in Bian et al., 2017). The fine mode bin for nitrate is simulated using the thermodynamic equilibrium model Regional Particulate Model Aerosol
 165 Reacting System (RPMARES) (Saxena et al., 1986) for the gas phase, aqueous chemical cycling of nitrate gas-aerosol
 partitioning in a system of $SO_4^{2-} - NO_3^- - NH_4^+ - H_2O$ (Table 2 in Bian et al., 2017), and a first order heterogenous reaction
 of HNO_3 on mineral dust and sea salt. The two coarse mode bins form from heterogenous production only. Additional tracers
 are included for ammonia (NH_3) and the ammonium ion (NH_4^+) that are necessary for the SO_4^{2-} - NO_3^- - NH_4^+ - H_2O system.
 Biomass burning, anthropogenic, and oceanic emissions of NH_3 prescribed from emission datasets (Table 2). Precursor gases
 170 for sulphate and nitrate are prescribed based on a prior MERRA-2 replay coupled to the GMI stratosphere-troposphere
 chemical mechanism (MERRA-2 GMI; Strode et al., 2019).

Table 1. Summary of aerosol emissions in the GOCART-2G benchmark simulation. GOCART-2G can be run with differing emissions sources and dataset resolutions if desired.

Emission Type	Species	Source	Temporal Resolution	Spatial Resolution
Anthropogenic (including ship and aircraft)	OC, BC, SO_2 , SO_4 , NH_3	CEDS (doi: 10.5281/zenodo.4741285)	Monthly	0.5° , downscaled to 0.15625°
Biomass Burning	BR, BC, SO_2 , NH_3	QFED v2.5r1 (Darmenov and da Silva, 2015)	Daily, with a fixed diurnal cycle based on latitude	0.1°
Volcanic	SO_2	Carn et al. 2017	Daily Eruptive and Outgassing	Point-sources
Dust	DU	Wind driven (Ginoux et al., 2001)	Model	Model Resolution
Sea Salt	SS	Wind driven (Gong, 2003; Jaegle et al., 2011)	Model	Model Resolution
Species prescribed for aerosol chemistry	H_2O_2 , OH, NO_3 , HNO_3	MERRA-2 GMI (Strode et al, 2019)	Monthly	0.5° x 0.625°
	DMS	Lana et al. (2011); Liss and Merlivat (1986)	Monthly	0.5° x 0.625°
	Open Ocean NH_3	Bouwman et al. (1997)	Monthly	0.5° x 0.625°

175

Table 2. Summary of aerosol parameterizations in GOCART-2G

Function	Specie(s)	Parameterization
Boundary Layer Turbulent Mixing	All	Lock et al., 2000; Louis, 1979
Moist Convection	All	Grell and Freitas, 2014
Settling Velocity	All	Fuchs, 1964
Dry Deposition	All	Wesely, 1989

Wet Deposition	All	Giorgi and Chameides, 1986; Balkanski, et al. 1993; Liu et al., 2001
Optical Properties	All	Hess et al., 1998; Colarco et al., 2014; Colarco et al., 2017
Sulphate Chemistry	Sulphate	Chin et al. 2000
Nitrate Chemistry	Nitrate	Bian et al. 2017; Saxena et al., 1986

Optics look up tables (LUTs) to convert from the simulated aerosol masses to optical quantities such as aerosol optical depth (AOD) are derived from Mie (spherical) calculations using parameters from the Optical Properties of Aerosols and Clouds (OPAC; Hess et al., 1998) and as described in Chin et al. (2002) and Colarco et al. (2010), except for dust, which is based on Colarco et al. (2014), and for brown carbon (see below). Optical properties are a function of aerosol species, particle size, and relative humidity (except for dust, which is assumed hydrophobic). From an optics perspective, hygroscopic growth occurs based on a specified growth factor as listed in the Appendices of Kemppinen et al. (2022). The resulting optics tables are available for download at <https://portal.nccs.nasa.gov/datashare/ies/aerosol/AerosolOptics/> (last access 5 December 2022) and the versions used in the initial release of GOCART-2G are given in Table A2. These high spectral resolution tables are useful for computing diagnostic optical quantities like AOD and backscatter, as shown later. They are also available in an aggregated format to provide optical properties needed to compute aerosol forcing at the spectral bands used in the model's radiative transfer code, RRTMG (Clough et al., 2005; Iacono et al., 2008).

2.2 Updates ~~to Aerosol Speciation~~ Incorporated into GOCART-2G

Three major changes with regards to aerosol speciation were implemented as part of GOCART-2G to either represent processes that were previously not included or improve the interaction between aerosols and radiation. 1) Brown carbon was added as a new radiatively active sub-species of carbon. This was done to account for differences in absorption properties between organic carbon emitted by biomass burning (from QFED) and anthropogenic sources (from CEDS), as described by Colarco et al. (2017). 2) Secondary organic aerosol (SOA) is now used to form brown and organic carbon from volatile organic carbon (VOC). Finally, 3) a mechanism to produce sulphate in the stratosphere (StratChem; Nielson et al., 2017) has been added to simulate sulphate more realistically at higher levels. StratChem is too computationally expensive to employ in a near real time system like GEOS FP but ~~can~~ may be appropriate for -reanalysis, hindcast, or other be used for research purposes. Additional details pertaining to these updates are given in the remainder of this section.

2.2.1 Implementation of Primary Organic Aerosol

Beginning with GOCART 2G, a distinction is made between “non-absorbing” anthropogenic and “absorbing” (also referred to as “brown”) biomass burning organic aerosol. Anthropogenic emissions of organic carbon, which are emitted based on CEDS, are solely considered to be “non-absorbing” organic carbon, with spectral optical properties that follow the OPAC

205 database and are as in Chin et al. (2002) and Colareo et al. (2010). Biomass burning emissions of organic carbon from the Quick Fire Emissions Dataset (QFED) are considered absorbing “brown” carbon and assigned optical properties that have spectrally varying absorption at wavelengths shorter than 550 nm as described in Colareo et al. (2017). This distinction was found in Colareo et al. (2017) to improve the comparison of the absorbing aerosol sensitive aerosol index between the model and data retrieved from the Ozone Monitoring Instrument (OMI) onboard the NASA Aura spacecraft. The optical properties between our absorbing and non-absorbing organic aerosol components are identical at wavelengths equal to and greater than 550 nm and treated by identical chemical and loss processes in the model.

210 2.2.2 Implementation of Secondary Organic Aerosol

A simplified SOA mechanism is employed that scales VOC emissions in terms of carbon monoxide (CO) emissions from anthropogenic and biomass sources. Following Kim et al. (2015) we assume production of anthropogenic VOC at a rate of $0.069 \text{ g (g CO)}^{-1}$ and biomass burning VOC at a rate of $0.013 \text{ g (g CO)}^{-1}$. The VOC tracers are advected and assumed to convert to SOA via reaction with the prescribed MERRA-2 GMI OH fields with a rate constant of $1.25 \times 10^{-11} \text{ cm}^3 \text{ molecule}^{-1} \text{ sec}^{-1}$ (Hodzic and Jimenez, 2011). The SOA produced is apportioned to the hydrophilic modes of organic (anthropogenic) and brown (biomass burning) carbon. Biogenic aerosols VOCs, including isoprene, monoterpene, and other terpenes are provided from the Model of Emissions of Gases and Aerosols from Nature (MEGAN; Guenther et al., 2012) and enter the model through the Harvard NASA Emission Component software (HEMCO, Keller et al., 2014) and are assigned to the hydrophilic mode of the organic carbon component. Unlike anthropogenic and biomass burning SOA that are produced in the air via the reaction of VOCs and OH, biogenic SOA is produced by scaling MEGAN emitted VOCs at the point of emission.

220 2.2.3 Implementation of Stratospheric Sulphate Aerosol

— An optional simplified stratospheric sulphate mechanism is implemented following the mechanism described in English et al. (2011). A tracer for carbonyl sulphide (OCS) is added to the model with a specified surface mixing ratio boundary condition of 490 pptv. OCS is largely inert in the troposphere and the model has been spun up so that a well-mixed distribution is achieved. Photochemical destruction of OCS is managed by the stratospheric chemistry package StratChem described in Nielsen et al. (2017). The reactions considered include binary consumption of OCS by OH and atomic oxygen, $\text{O}(^3\text{P})$, and photolytic destruction of OCS (the dominant process), using rate constants from Sander et al. (2011). The sulphur is assumed oxidized to SO_2 and then passed to GOCART, which computes the sulphate aerosol production using the same series of reactions as above for the tropospheric sulphate aerosol production. This mechanism provides us a simplified representation of the naturally occurring background stratospheric sulphate. While this mechanism is included in the benchmark experiment analysed in Section 4, it is currently not intended for use in a typical model simulation such as what is used to produce GEOS FP.

230 2.3 Code Refactoring

A major refactoring of the GOCART source code was completed to improve performance, flexibility, and code quality within GOCART-2G. [This was essential to allow for future development of the aerosol module and for the code to be](#)

effectively shared with external organizations. The code refactoring itself is intended to produce identical results, within roundoff errors, to the legacy GOCART code. GOCART has been split into its own repository (<https://github.com/GEOS-ESM/GOCART.git>) with specific low-level interfaces that do not depend on the Earth System Model Framework (ESMF, <https://earthsystemmodeling.org>) and are independent of the overall GEOS architecture. This allows for code to be effectively shared with external organizations. Performance was enhanced through optimization of settling and nitrate chemistry parameterizations, eliminating extraneous calculations, and removing known bugs. The other code refactoring consisted of eliminating non-standard Fortran, eliminating redundant and legacy constructs, reducing duplicated logic within and across components, implementing cleaner component resource files, improving procedure and variable names in the source code to make the intent obvious to users and developers, and splitting large procedures with well-defined responsibilities.

————— A large component of the refactoring involved more widespread adoption of the ESMF within the parent GOCART-2G component. Improved flexibility within the code is essential for future development of GOCART-2G within GEOS. Carbon, sulphate, nitrate, sea salt, and dust, now have their own ESMF components and can instantiate multiple active and/or passive instances at one time; an active instance participates in the physical coupling with the host model. For example, carbonaceous aerosol is one of GOCART-2G's children and black, brown, and organic carbon are each run as an active instance of the carbonaceous aerosol component. This means that the model is provided with characteristics of each carbon species, including optics, density, particle radius, and the fraction that enters as hydrophobic, and black, brown, and organic carbon utilize the same code to perform process-related calculations, thus eliminating duplicated code. An example of a passive instance that could be run using the same methodology would be to track and provide diagnostics for the portion of a species from a specific emission source, such as sulphate formed from in response to volcanic emissions.

An important improvement in terms of flexibility was the addition of user supplied wavelengths for aerosol diagnostics. Previously, GOCART provided aerosol optical properties at the specific bands required by the radiation package, but diagnostic file output was restricted to the 550 nm wavelength. To better support data assimilation of multi-wavelength aerosol data, the model is now able to directly output aerosol optical properties at multiple wavelengths without the need for an offline utility. The model is also able to output stratospheric AOD using the GEOS tropopause height. Additional details on the code changes and refactoring are in the supplemental document.

3 Observational Datasets Used for Model Evaluation

3.1 Moderate Resolution Imaging Spectroradiometer (MODIS) Neural Net Retrieval (NNR)

Here we evaluate AOD at 550 nm in GOCART-2G using observations from Collection 6.1 of the Moderate Resolution Imaging Spectroradiometer (MODIS) aboard the Aqua satellite (Levy et al., 2015). The particular MODIS dataset used for this evaluation is the Neural Net Retrieval (NNR) described in Section 3.2.2 of Randles et al. (2016), which bias corrects and homogenizes MODIS observations to be consistent with AERONET. THE NNR algorithm relies on cloud-cleared, gas-corrected reflectances used by the Deep Blue (Sayer et al., 2019) and Dark Target (Remer et al., 2020) retrievals and uses a

neural net trained on co-located AERONET direct sun AOD measurements. The monthly mean NNR AOD retrievals are obtained by a weighted average based on the number of pixels available for a given 0.25° latitude by 0.3125° longitude grid box. The same NNR-based analysis was also carried out for the Terra satellite, complemented by additional measurements from the Multi-angle Imaging SpectroRadiometer (MISR); these results are presented in the supplemental material. GEOS has been sampled such that model data is only included when and where MODIS observations are available at the three hourly timestep of the MODIS NNR product.

3.2 AERONET

The Aerosol RObotic NETwork (AERONET) is a collection of ground-based stations equipped with Cimel sun photometers for measuring spectral sun irradiance and sky irradiances (Holben et al., 1998). Under cloud-free conditions, AOD is computed as the total optical depth measured by the sun photometer minus the contribution from Rayleigh scattering and trace gases. For comparison to GEOS, Version 3 of the Level 2 product, which includes cloud screening, is utilized (Giles et al., 2019). Although AERONET provides spectrally varying AOD, only AOD at 550 nm is examined in addition to the Angstrom exponent computed using 470 nm and 870 nm. For stations that do not report AOD at 550 nm, the Angstrom exponent for 440 nm and 675 nm is used to convert the AOD at 500 nm to 550 nm.

3.3 OMPS-LP

The Ozone Mapping and Profiler Suite (OMPS) aboard the Joint Polar Satellite System (JPSS) Suomi National Polar-orbiting Partnership (S-NPP) satellite contains a limb profiler (LP) that can observe aerosol with-in the stratosphere. Stratospheric AOD at 869 nm is evaluated using observations from OMPS-LP (Taha et al., 2021) to validate volcanic eruptions and pyrocumulonimbus (PyroCB) reaching the stratosphere. The data from OMPS LP are presented as the daily, zonal mean of the stratospheric AOD, evaluated by integrating the retrieved extinction from the GEOS-derived tropopause altitude to the 40 km top altitude of the OMPS LP retrievals. Data are not available during periods of instrument issues and under low/no-sun conditions (e.g., polar night). Although the algorithm includes cloud screening, some polar stratospheric clouds are evident in the dataset, as shown below.

3.4 CALIOP

Since 2006, the Cloud Aerosol Lidar with Orthogonal Polarization (CALIOP), aboard NASA's CALIPSO ATrain satellite (Winker et al., 2007, 2009), has provided insights about aerosol vertical structure. For this study, the highest-quality lidar Level 1.5 standard data product version V1.00 was employed (NASA, 2019): a cloud-cleared dataset with a 20 km horizontal and 60 m vertical resolution for a height up to 20.2 km. The observations include contributions from both aerosols and gas molecules (Rayleigh scattering), so our analysis is limited to the total (aerosols + molecular) attenuated backscatter coefficient.

3.5 Surface Particulate Matter from IMPROVE and EMEP

Like in Buchard et al. (2016) and Provençal (2017), surface aerosol mass is evaluated over the United States using data provided by the Interagency Monitoring of Protected Visual Environments (IMPROVE, <http://vista.cira.colostate.edu/Improve/>) Program and over Europe using data from the European Monitoring and Evaluation Programme (EMEP, <https://ebas.nilu.no/>). IMPROVE and EMEP monitoring sites are typically located in rural areas representative of the region and with minimal influence from localized urban pollution. Following the module description for the IMPROVE network (Hand et al., 2011), PM_{2.5} in GOCART-2G was computed using the equation below for aerosol with an aerodynamic diameter of 2.5 microns (Collow et al., 2023). Variable names in the equation are consistent with those given in the file specification document for GEOS Forward Processing (Lucchesi, 2018). The multiplication factors of 0.9614 for bin 1 of dust and 0.3871 for bin 3 of sea salt account for a conversion to aerodynamic diameter and the fact that only a portion of the bin is smaller than 2.5 microns. Though not done here, other studies have used the entirety of bin 1 for dust in comparison to IMPROVE observations due to a wide range in the shape factor for dust (Kim et al., 2021).

310

Reconstructed PM_{2.5} is given by

$$\begin{aligned} \text{PM}_{2.5} = & 0.9614 * \text{DU001} + f_{\text{ss,rh}} * (\text{SS001} + \text{SS002} + 0.3871 * \text{SS003}) + \\ & \text{OCPHOBIC} + \text{BCPHOBIC} + \text{BRPHOBIC} + f_{\text{oc,rh}} * \text{OCPHILIC} + \\ 315 \quad & + f_{\text{bc,rh}} * \text{BCPHILIC} + f_{\text{br,rh}} * \text{BRPHILIC} + f_{\text{su,rh}} * \text{SO4} + f_{\text{ni,rh}} * \text{NH4a} + f_{\text{ni,rh}} * \text{NO3an1} \end{aligned}$$

where the growth factor with relative humidity, $f_{x,rh}$, for each species is calculated as

$$f_{x,rh} = 1 + \left(\left(\left(\frac{r_{rh}}{r_0} \right)^3 - 1 \right) \times \frac{\rho_{\text{Water}}}{\rho_{\text{Dry Species}}} \right)$$

320 using the radius specified for a given relative humidity from the optics files listed in Table 4 as r_{rh} and the radius at 0% relative humidity for r_0 .

Following their respective documentations, PM_{2.5} for the IMPROVE sites in the United States was computed using a relative humidity of 35% (Hand et al., 2011) while PM_{2.5} for the EMEP sites in Europe was computed using a relative humidity of 50%. GEOS was sampled according to when and where observations were available. Note that IMPROVE observations are collected every three days while data from EMEP ranges in temporal frequency from one hour to six days. EMEP observations are also not homogeneous with respect to the instruments and measurements of individual aerosol species at each site.

4 Evaluation of GOCART-2G

A benchmark simulation for GOCART-2G was carried out for the period of 2016 through 2019 using GEOS Release 10.23.0 (<https://github.com/GEOS-ESM/GEOSgcm/releases/tag/v10.23.0>, last accessed: November 21, 2023) on a cubed-sphere c180 grid (~0.5° spatial resolution) with 72 vertical levels. Meteorology, particularly atmospheric temperature, specific humidity, and winds were replayed to the analysis from MERRA-2 (Gelaro et al., 2017), while boundary conditions for sea surface temperature and sea ice concentration were from the Reynolds analysis (Reynolds et al., 2002). [The benchmark simulation uses a one moment microphysics scheme such that aerosols are not used as cloud condensation nuclei for the formation of liquid or ice clouds.](#) Two pyroCb events were included in the simulation for British Columbia in 2017 (Torres et al., 2020; Das et al., 2021) and Australia in late December 2019 (Schwartz et al., 2020), [and the StratChem mechanism is turned on to provide necessary mechanism for simulation of the stratospheric sulphate layer.](#) There is no assimilation of aerosol optical depth or observational constraint for aerosol extinction or mass. Therefore, all observations used for comparison are independent from the model simulation. [Additional one-year simulations, overlapping for 2016, were completed using the legacy GOCART configuration of GEOS as well as GOCART-2G without the stratospheric sulphate mechanism. The legacy GOCART configuration](#) ~~Aside from~~ [lacks the code and configuration changes described in Section 2, the legacy GOCART configuration and uses](#) ~~used~~ [an older dataset for anthropogenic emissions as described in Randles et al. \(2017\).](#)

4.1 Aerosol Mass Budget

Emissions and production from each aerosol species are presented in Figures 1 and 2, [while details pertaining to the global mass budget can be found in Table 3.](#) Wind-driven dust is emitted primarily over Saharan Africa, Saudi Arabia, the Asia deserts, the Simpson desert of Australia, and the southern tip of South America (Figure 1a), in agreement with Colarco et al. (2010), Randles et al. (2017) and Rémy et al. (2019). The seasonal cycle of dust emissions peaks in boreal spring and is minimized during the fall months (Figure 2a). [An increase in dust emissions is present in GOCART-2G relative to legacy GOCART due to an intentional increase in the emissions scaling factor to match the global mean AOD for dust of 0.028 from Kok et al. \(2021\).](#) Most dust is deposited near the source regions, however there is notable transport of Saharan dust across the Atlantic Ocean (Figure 3a).

[Table 3. Global annual mean mass budget for emission and/or production, lifetime, and burden of aerosols in GEOS-Legacy GOCART and GEOS-GOCART2G for the period of 2016 through 2019 for 2016 and GEOS-GOCART-2G for 2016 through 2019.](#)

	Legacy GOCART (2016)	GOCART-2G w/o StratChem (2016)	GOCART-2G (2016)	GOCART-2G (2016-2019)
Brown Carbon Emissions [Tg yr⁻¹]	n/a	63.58	63.63	4565.08
Brown Carbon Lifetime [days]	n/a	5.76	5.76	6.02
Brown Carbon Burden [Tg]	n/a	0.99	0.99	1.07±

Brown Carbon AOD	n/a	0.012	0.012	0.013
Black Carbon Emissions [Tg yr⁻¹]	10.27	9.62	9.62	9.62
Black Carbon Lifetime [days]	6.47	6.57	6.57	6.70
Black Carbon Burden [Tg]	0.18	0.17	0.17	0.187
Black Carbon AOD	0.004	0.003	0.003	0.004
Dust Emissions [Tg yr⁻¹]	1114	1752	1752	13961726
Dust Lifetime [days]	5.27	5.49	5.49	5.46
Dust Burden [Tg]	16.07	25.66	25.66	26.1725.27
Dust AOD	0.019	0.029	0.029	0.028
Nitrate Production [Tg yr⁻¹]	101.15	137.60	137.62	4.5139.88
Nitrate Lifetime [days]	3.8	3.23	3.23	3.28
Nitrate Burden [Tg]	0.33	0.52	0.52	0.543
Nitrate AOD	0.003	0.005	0.005	0.006
Organic Carbon Emissions [Tg yr⁻¹]	94.71	99.00	99.00	96.97
Organic Carbon Lifetime [days]	5.51	4.15	4.15	4.33
Organic Carbon Burden [Tg]	1.42	1.11	1.11	1.14
Organic Carbon AOD	0.018	0.017	0.017	0.017
Sulphate Emissions/Production [Tg yr⁻¹]	127.85	120.91	121.06	78118.4
Sulphate Lifetime [days]	3.594.13	3.54	4.30	4.55
Sulphate Burden [Tg]	1.2443	1.16	1.41	1.464
Sulphate AOD	0.03	0.028	0.03	0.031
Sea Salt Emissions [Tg]	4582	4581	4581	45122152
Sea Salt Lifetime [days]	0.8256	0.82	0.82	0.82
Sea Salt Burden [Tg]	10.328.70	10.25	10.25	10.4610.08
Sea Salt AOD	0.036	0.036	0.036	0.036

355 Sea salt emissions are enhanced along the northern and southern hemisphere storms tracks as well as the Intertropical Convergence Zone (ITCZ), with little variability across the seasonal cycle. While the spatial pattern is similar, sea salt emissions have decreased from MERRA-2 (Randles et al., 2017). In a correction since MERRA-2, sea salt is not emitted over the Great Lakes or Caspian Sea. Most sea salt is emitted in the coarse mode, with the largest contribution from bin 3 (mode radius of 2.4 μm). Relative to the largest three bins, emissions from bins 1 and 2 are negligible to the total mass (Figure 2b). Nearly all sea salt is deposited over the ocean, in elevated quantities over the storm tracks and ITCZ (Figure 3b). [The global](#)

360 [mean AOD for sea salt did not change with the version of GOCART and remains slightly below the median relative to other AeroCom Phase III models.](#)

Carbonaceous aerosol is emitted over land (Figure 1b-d), with a seasonal cycle that peaks in the boreal summer due to the temporal variability in biomass burning (Figure 2c-d). Anthropogenic emissions account for, on average, 62% of the total black carbon emissions and 21% of the organic aerosol emissions. Brown carbon, emitted through biomass burning, ranges from 37% to 65% of the monthly emissions of organic aerosol. There is also a contribution of brown carbon produced from SOA. [Due to the mechanism for biogenic emissions introduced in GOCART-2G, there is an increase in the total emissions of organic matter relative to legacy GOCART. Subsequently, there is an increase in burden for total organic and brown carbon, that is near the median for the AeroCom Phase III models.](#)

Sulphate is directly emitted within GEOS from the anthropogenic emissions and has a contribution that is produced from the oxidation of dimethyl sulphide (DMS), methane ~~sulfonic~~-sulphonic acid (MSA), and sulphur dioxide (SO₂). Emission and production of sulphate is maximized in densely populated areas including China, India, Europe, and the Eastern United States (Figure 1e). Anthropogenic emission of SO₂ is the largest contribution to sulphate production and is responsible for the subtle downward trend of sulphate production over the four-year timeseries. The summertime peaks in sulphate production during 2018 and 2019 are in response to the explosive volcanic eruptions of Kilauea in May 2018 and Raikoke in June 2019 (Figure 2e) while the broader summertime peaks in gaseous production of sulphate are associated with biomass burning emissions of SO₂. [There is a small impact of the stratospheric sulphate mechanism on the total burden and AOD for sulphate.](#)

Nitrate aerosol is not directly emitted. Most nitrate forms in response to heterogenous production on dust and sea salt aerosols (Figure 2f). A somewhat bimodal seasonal cycle in the production of nitrate occurs due to spring and fall peaks in the emission of ammonia (NH₃). Due to the anthropogenic and agricultural nature of ammonia emissions, the spatial pattern of nitrate deposition is very similar to that for organic and brown carbon. Most nitrate aerosol is deposited close to the source while some is transported over the ocean by the atmospheric circulation (Figure 3f). [An increase in nitrate production in GOCART-2G relative to legacy GOCART resulted in an overall increase in the nitrate burden and optical depth. This is likely in response to the newer emissions and a change in the input dataset for the oxidant fields relevant for nitrate chemistry.](#)

385 4.2 Comparison to Observational Datasets

4.2.1 Satellite Based Aerosol Optical Depth

A broad, global comparison of the AOD between MODIS [Aqua](#) and [both versions of GOCART/GEOS for 2016](#) is shown in Figure 4. [Over the ocean there is little difference in the annual mean AOD between legacy GOCART and GOCART-2G, and the model generally performs well over the ocean relative to MODIS \(Figure 4a-c\).](#) However, there are notable biases [and differences between the model versions](#) over land (Table 4). [Most notably, AOD increased in the model over northern South America, Africa, Saudi Arabia and southern Asia. While this increase led to an improvement in AOD compared](#)

395 to MODIS over South America and southern Asia, there are indications that an increase in dust led to a degradation in
 GOCART-2G elsewhere. AOD is too high in GEOS across northern Africa and Saudi Arabia, suggesting there could be too
 much dust in the model. Although smaller in magnitude, the overestimate in AOD extends into the central Atlantic due to
 400 transported dust. A positive bias in AOD with GOCART-2G is present across Saudi Arabia and northern Africa, extending
 over the central Atlantic, presumably from transported dust. The positive bias in AOD is larger in magnitude when GEOS with
 GOCART-2G is compared to MODIS aboard Terra relative to Aqua and suggests there could be a further issue with the diurnal
 cycle of dust emissions as Terra has a morning overpass while Aqua has an afternoon overpass (Figure S2). However, this
 positive bias in AOD in dusty regions is not as large when GEOS with GOCART-2G is compared to MISR, also aboard Terra
 405 and so with the same diurnal sampling. (Supplemental Figure S3) or AERONET (Figure 9, shown later). Conversely, a negative
 bias in AOD is present in the northern hemisphere boreal regions that is larger in magnitude when the comparison is made to
 Aqua. In general, the AOD over land is larger for Aqua than Terra in the MODIS NNR product (Table 4), in disagreement
 with what is presented by Levy et al. (2018) for the dark target algorithm similar in magnitude but opposite in sign from what
 was reported for the standard MODIS algorithm products in Levy et al. (2018).

Table 4. Global annual mean AOD at 550 nm for 2016 in legacy GOCART, GOCART-2G, and the satellite-based datasets as well as for the period of 2016 through 2019 in the GEOS-GOCART2G model and the satellite-based datasets.

	<u>Observation</u> (2016)	<u>Legacy</u> <u>GOCART (2016)</u>	<u>GOCART-2G</u> (2016)	<u>Observation</u> (2016-2019)	<u>GOCART-2G</u> (2016-2019)
<u>MODIS NNR Terra</u> (Global)	<u>0.1349</u>	<u>0.1093</u>	<u>0.1373</u>	<u>0.1272</u>	<u>0.1395</u>
<u>MODIS NNR Terra</u> (Ocean)	<u>0.1067</u>	<u>0.0933</u>	<u>0.1066</u>	<u>0.0980</u>	<u>0.1088</u>
<u>MODIS NNR Terra</u> (Land)	<u>0.18399</u>	<u>0.14020.1389</u>	<u>0.1939</u>	<u>0.1786</u>	<u>0.1961</u>
<u>MODIS NNR Aqua</u> (Global)	<u>0.1415</u>	<u>0.1093</u>	<u>0.1372</u>	<u>0.1360</u>	<u>0.1392</u>
<u>MODIS NNR Aqua</u> (Ocean)	<u>0.1081</u>	<u>0.0924</u>	<u>0.1057</u>	<u>0.0996</u>	<u>0.1077</u>
<u>MODIS NNR Aqua</u> (Land)	<u>0.2013</u>	<u>0.1407</u>	<u>0.1956</u>	<u>0.2015</u>	<u>0.1974</u>
<u>MISR (Global)</u>	<u>0.1606</u>	<u>0.1198</u>	<u>0.1397</u>	<u>0.1612</u>	<u>0.1414</u>
<u>MISR (Ocean)</u>	<u>0.1294</u>	<u>0.0999</u>	<u>0.1090</u>	<u>0.1301</u>	<u>0.1107</u>
<u>MISR (Land)</u>	<u>0.2172</u>	<u>0.1521</u>	<u>0.1949</u>	<u>0.2175</u>	<u>0.1967</u>

Monthly mean timeseries of global mean AOD over ocean, in addition to the mean seasonal cycles, can be found in Figure 5. In the top two panels, the solid black line represents the MODIS [Aqua](#) observations while the coloured shading accumulates the optical depth for each aerosol species in GEOS. Though difficult to see in the global spatial map, it is evident that AOD is underestimated in the model over the ocean, [and this bias has been reduced in GOCART-2G \(Figure 5c\)](#). There is a seasonal cycle in the bias such that it is maximized during the months of March, September, and October and minimized during the boreal summer and winter (Figure 5d). MODIS indicates a bimodal seasonal cycle for total AOD ([Figure 5b](#)), with one peak in the Northern Hemisphere late winter and early spring that is not present in GEOS, and another during the summer that persists later into the season than in the model. The largest contribution to the total AOD comes from sea salt and in agreement with the fact that emissions cover a large fraction of the domain, there is little temporal variability in the optical depth for sea salt. Peaking in April, nitrate makes up the smallest contribution to the total AOD over the ocean. Peaks in sulphate are present in the boreal summers of 2018 and 2019, coincident with peaks in the gaseous production of sulphate due to large volcanic eruptions as shown in Figure 2e.

The analysis of AOD over land is broken down into eight continental scale regions. A spatial map demonstrating the geographic extent of each region is in the supplemental document (Figure S5). Beginning with North Africa in Figure 6a, the region is dominated by dust that typically peaks in the spring and summer months. GEOS can produce the observed temporal variability in AOD; however, the magnitude of AOD is higher than MODIS throughout the entire timeseries. This is likely due to an overestimate of dust emissions [in GOCART-2G](#).

GEOS underestimates the AOD in South Asia, North America, South America, Siberia, and Europe (Figure 6d-h). The Americas, Siberia, and South Asia are influenced by biomass burning aerosol. Biomass burning aerosol is often underestimated in models, including GEOS, and in many cases have errors due to assumptions made for the particle properties (Zhong et al., 2022 and references within). Collow et al. (2022) demonstrated the GEOS struggles to match the observed mass extinction efficiency within a smoke plume. It is likely that the negative bias in these regions is in response to biomass burning aerosol. Europe and South Asia are more complicated due to higher relative proportions of dust and sulphate. Dust emissions are tuned in GEOS using a global metric. It is therefore plausible that there are errors in the transport of dust to Europe and the overall life cycle of dust from Asian deserts such as the Gobi and Taklamakan Deserts. A lack of the negative bias in AOD over South Asia in comparison to Terra indicates the underestimation of AOD in GEOS contains a diurnal cycle (Figure S6d).

GEOS completely misses the observed seasonal cycle in AOD over Europe, [regardless of the version of GOCART](#). For this reason, Europe was further divided into subregions as indicated by Figure 7 (See Figure S8 for the geographical depiction of the subregions). There is decent agreement [with respect to the annual cycle](#) in AOD between MODIS and GEOS over the Iberian Peninsula and Scandinavia. Conversely, [the GEOS model](#) does not capture the summertime maxima in AOD

across central Europe or the United Kingdom. This will be further elaborated upon through a comparison with AERONET observations in Section 4.2.2 and an evaluation of surface mass in Section 4.2.4.

445 There is remarkable agreement in the AOD over South Africa and Australia with GEOS capturing the seasonal cycle and magnitude from the observations (Figure 6b-c). The fact that South Africa is also dominated by biomass burning aerosol but does not have the negative bias seen in other biomass burning regions suggests there could be an overestimate of AOD due to another species, ~~or~~ that the optical properties for brown and organic carbon in GEOS are better suited for the fuel types burned in Africa rather than the boreal forests of North America and Siberia and the rainforests of South America, or that emissions are easier to retrieve in this region.

450

4.2.2 AERONET

Representative AERONET stations were selected for evaluation based on a comparison among dozens of stations in North America, Europe, and northern Africa. Due to the poor agreement in the seasonal cycle of AOD in Europe between GEOS and MODIS, Mainz, Germany was selected as the site demonstrates characteristics of others in the area. The AERONET 455 site is adjacent to both rural and urban landscapes and is in a moderately to highly polluted region. In agreement with the comparisons to MODIS, GEOS tends to underestimate the AOD with respect to the AERONET observations and has a mean negative bias of 0.28, in log space, that tends to be larger in magnitude during the summer months (Figure 8). In addition to smaller values of AOD occurring more frequently in GEOS compared to the observations, there is also less variability in the AOD. GEOS has a better agreement for the Angstrom Exponent, computed using 440 nm and 675 nm, accurately having the 460 dominant aerosol in the fine mode. Potential reasons for the underestimate in AOD may be ~~a lack of emissions from smaller scale sources that are not represented in the~~ due to uncertainties in the CEDS dataset (McDuffie et al., 2020) or insufficient biomass burning aerosol that is transported from North America.

Comparisons between GEOS and AERONET stations across northern Africa and Saudi Arabia are consistent with respect to the mean bias in the model relative to MODIS NNR. Tamanrasset was chosen for additional evaluation since it is in 465 northern Africa where GEOS overestimates AOD compared to MODIS (Figure 9). The AERONET site is in the highlands of the Algerian Sahara, away from industrial activity, making dust the primary aerosol species. Here, there is a positive mean bias in the modelled AOD of 0.18 and a reasonable correlation between GEOS and AERONET of $R=0.84$, computed using $\log(\text{AOD}+0.01)$ (Figure 9b). GEOS overestimates the AOD when the AERONET observations lie between 0.1 and 0.5 as demonstrated in Figure 9b. Agreement between the model and observations is not as good for the Angstrom exponent as the 470 correlation is only 0.48 and there is a mean bias of -0.15, indicating that aerosol in the model is often coarser than seen by AERONET.

As shown in the comparison to MODIS, Southern Africa is dominated by biomass burning aerosol. Mongu, located in central south Africa within Zambia, was selected as a representative site for smoke. Despite good agreement between GEOS and MODIS on a continental scale for Southern Africa, there is considerable underestimation in AOD within the model when

475 compared to AERONET at a local scale (Figure 10a and b). This is especially the case for the southern hemispheric winter months when biomass burning is prevalent. The correlation of 0.85 at Mongu is on par with what was reported for the M2Replay, a MERRA-2 like simulation without the assimilation of AOD, in Randles et al. (2017). As shown by the kernel density estimate in Figure 10b, the correlation between the observations and GEOS is weaker for lower values of AOD. GEOS has a smaller amplitude in the Angstrom exponent such that there is an underestimate during the southern hemisphere summer months (Figure 10c). GEOS is likely correctly characterizing the July peaks in AOD as biomass burning aerosol but is missing coarse mode aerosols, perhaps dust, during the warmer months.

The AERONET station in Langley, Virginia demonstrates behaviour typical of other stations and is close to the national average timeseries for AOD across the United States. Located on the southern tip of the Chesapeake Bay less than 40 km from Norfolk, Virginia, the Langley AERONET site often experiences urban and marine aerosol regimes, with occasional intrusions of smoke and dust. At this station, GEOS overestimates the lower values of AOD and underestimates the higher values of AOD (Figure 11a), giving a poorer correlation than at the sites in Europe and the Sahel (Figure 11b). GEOS does not have as much variability in the Angstrom exponent as the observations but accurately represents that there is fine mode aerosol. A summary for 77 AERONET stations across the United States and Canada is given in the form of a kernel density estimate in Figure S12. Numerous stations underestimate AOD during the summer months, in agreement with the MODIS evaluation. Exceptions to this are stations in the desert southwest including Tucson, Flagstaff, Table Mountain CA, and USC, where GEOS simulates higher AOD than AERONET. These stations are characterized by a measured AOD below national average (Figure S11).

4.2.3 OMPS-LP Stratospheric AOD

Newly added diagnostics in GOGART-2G include total aerosol scattering and extinction in the stratosphere, which allows for comparison to observations from OMPS-LP. Figure 132 shows the daily, zonal mean stratospheric AOD at 870 nm from OMPS LP (panel a) and the GEOS simulation (panel b). GEOS modelled fields are masked where OMPS LP does not report retrievals either due to polar night conditions, scattering angle filtering, or missing data from spacecraft operations issues. Note some high AOD values along the northernmost points hugging the polar night line, particularly evident in January; these are unfiltered polar stratospheric cloud artifacts present in the OMPS LP data set (Ghassan Taha, personal communication) not included in the GEOS simulation. Generally, the model reproduces the observed seasonal variability and magnitude of the stratospheric AOD and has markers for significant stratospheric perturbing events such as volcanic eruptions (Aoba in the tropics in 2018, Ulawun in the tropics in 2019, Raikoke at high northern latitudes in 2019) and pyrocumulonimbus events (notably the British Columbia fires in high northern latitudes in late 2017). Even the seasonal variability evident exiting polar night is well captured in the model. Persistence of volcanic plumes following events however is not well captured in the model, suggesting difficulties with vertical placement and so long-range transport.

4.2.4 Vertical Profile of Attenuated Backscatter

To assess the vertical structure of aerosols in the GEOS-GOCART-2G model, we selected four regions of particular interest, as defined by Buchard et al. (2017). These included the dust transport region from northern Africa to the North Atlantic, the biomass burning regions of southern Africa and the Amazon, and an area over the continental United States.

510 Figure 143 shows the June-July-August 2016 regional average of CALIOP 532 nm aerosol attenuated backscatter in black, and the corresponding attenuated backscatter sampled in space and time from GEOS-GOCART-2G in red (Supplemental figures S123-S165 show curtain plots of attenuated backscatter coefficients over the same regions). Generally, the GEOS-GOCART-2G attenuated backscatter profile tends to exhibit ~~comparable-similar~~ vertical structure as CALIOP in all four regions of study. Notably, GEOS-GOCART-2G attenuated backscatter values agree well with CALIOP values within the
515 CALIOP 25th-75th percentile range and their maximum values are located at around the same height. [GEOS-GOCART-2G overestimates attenuated backscatter near the surface and underestimates attenuated backscatter just above the boundary layer over the United States and South America regions, which may be due to insufficient convective transport between the boundary layer and free troposphere, or the lack of a plume rise parameterization for intense fires.](#)

As observed in our MERRA-2 study (Buchard et al., 2017), near-surface attenuated backscatter is underestimated
520 relative to CALIOP in the Northern and Southern African regions, particularly for sea salt type aerosols near the ocean (Figures S154-S156). This could be due to either errors in the aerosol mass or in the hygroscopic growth assumption during the conversion from aerosol mass to optical properties. Nonetheless, calibration errors in CALIOP needs also to be considered as they tend to accumulate near the surface, making it difficult to place too much confidence in CALIOP values near the surface.

4.2.5 Surface Mass

525 Across the United States, surface particulate matter is evaluated in [the GEOS-GOCART-2G model](#) relative to the IMPROVE network. GEOS overestimates PM_{2.5} throughout the entire period of 2016 through 2019 however the model is well correlated to the observations (Figure 145). The 2017 and 2018 wildfire seasons were particularly bad in the United States as indicated by the summertime maxima in PM_{2.5} in the IMPROVE observations and GEOS. The total fine surface matter is further divided into individual aerosol species in Figure 156. Like with the total PM_{2.5}, sulphate aerosol is consistently
530 overestimated in GEOS. The IMPROVE observations indicate a seasonal cycle in sulphate that peaks in the summer, which is muted in GEOS. GEOS also struggles with the seasonal cycle for fine mode nitrate, overexaggerating the summertime minimum and wintertime maximum. The largest contributor to the overestimate of PM_{2.5} in GEOS is organic carbon. During biomass burning events in the summers of 2017 and 2018, the mean surface concentration of organic matter in the model exceeds the mean plus one standard deviation in the observations. Although the sampling differs, AOD is underestimated with
535 respect to satellite observations during the same events (Figure 6e). This indicates either too much aerosol is at the surface and not transported higher in the atmosphere and/or the mass extinction efficiency for smoke is too low in the model. Dust suffers from the opposite problem. Both the mean and the variability are underestimated by GEOS, with the largest bias during the

summer months. Dust emissions were tuned for more prominent regions such as the Sahara Desert. It is likely the emissions are not representative for the soil conditions in the United States in addition to deficiencies in the long-range transport (Kim et al., 2019; Kim et al., 2021).

The European Monitoring and Evaluation Programme (EMEP) had 67 stations across Europe with PM_{2.5} data for the period of 2016 through 2019 however only a fraction of those also provided sulphate, nitrate, and carbon. There were no observations of dust available. Four representative stations within Germany and one in Poland have been selected due to their availability of data and consistency with instrumentation. GOCART-2G overestimates surface PM_{2.5}, especially during the winter months (Figure 167). This is the opposite bias from Provençal et al. (2017) which evaluated the MERRAero reanalysis, and there are multiple reasons as to why there could be a larger aerosol concentration in the GOCART-2G simulations (which do not assimilate aerosol data). Aside from investigating a later time period for a subset of stations, nitrate and brown carbon were not included in MERRAero, although data assimilation may have apportioned the mass adjustments to the represented species. Additionally, we used an aerodynamic diameter for the particle size and accounted for hygroscopic growth since the observations are acclimated to a relative humidity of 50% prior to being recorded, in contrast to the geometric diameter and assumption of dry aerosol used by Provençal et al. (2017). Relating the seasonal cycle of surface aerosol mass in Central Europe to the AOD in Figure 7d, there is an evident mismatch.

To further diagnose potential contributions to positive bias in PM_{2.5} over Europe, sulphate, nitrate, and carbon are evaluated. Like with PM_{2.5}, all species are overestimated by the model (Figure 178). Most easily seen by comparing the spread between the 25th and 75th percentiles, GEOS captures the seasonal cycle of nitrate, organic carbon, and black carbon to some extent. The late winter peak in nitrate occurs a month too early in the model with a drastic decrease in the spring, perhaps indicating an issue with the emissions. While the seasonal cycle of carbonaceous aerosols is exaggerated in GOCART-2G, it correctly predicts a summertime minimum and a November maximum in black carbon. Given that PM_{2.5}, sulphate, nitrate, and carbon are all overestimated in Europe, it is evident that there is a concern much larger than processes related to a single species, as was the case for the United States. With only five stations analysed, representativeness becomes a concern when comparing a single point to a box with a resolution of roughly 50 km. However, the site description for Melpitz, one of the stations used, states that the site is representative of the Central European background troposphere following comparison with multiple other sites (<https://gawsis.meteoswiss.ch/GAWSIS/#/search/station/stationReportDetails/0-20008-0-MEL>, last accessed 24 February 2023). Other plausible explanations include biases in the modelled planetary boundary layer height and aggressive hygroscopic growth to match a relative humidity of 50%.

5 Discussion

GOCART, the underlying aerosol module within the Goddard Earth Observing System (GEOS) underwent an overhaul that coupled science changes with a code refactoring to enable future development of modelled aerosols within the system. Primary science changes focused on ~~the introduction of the new radiatively active species, brown carbon,~~

570 ~~repartitioning of updates to carbonaceous aerosol, with organics now distinguished based on the emission sources- (brown~~
~~versus “white” organic aerosol), updates to the secondary organic aerosol production, and an observation-informed retuning~~
~~of the organic matter to organic carbon ratio for organic matter.- Sulphate was updated to accommodate an optional stratospheric~~
~~sulphate mechanism, as well as secondary organic aerosols.- As part of the new species To accommodate for brown carbon and~~
575 ~~secondary organic aerosols, MEGAN was coupled to HEMCO to provide biogenic emissions and the ratio of organic carbon~~
~~to particulate organic matter was revised.- Scientifically, no changes were made to dust, sea salt, or nitrate, or sulphate when~~
~~moving from the legacy GOCART code to GOCART-2G. Therefore, any biases in these species in GOCART-2G were either~~
~~inherited from prior versions of GOCART or introduced based on changes to emissions.~~

The modernization of GOCART-2G was necessary to enable future development. The use of multiple instances for a
single species is employed for the three sub-species of carbon. This development could be expanded upon in future versions
580 with, for example, ash as an additional instance of dust ~~owing to similar microphysical processes and optical properties~~. The
ability to have diagnostics provided in multiple user-selected wavelengths is particularly useful for aerosol assimilation and
facilitates the comparison of the model with other sensors, such as OMPS LP. At the present time, GEOS assimilates AOD at
550 nm. It is anticipated that additional wavelengths will be added for aerosol assimilation after GEOS transitions to a Joint
Effort for Data assimilation Integration (JEDI) based system. Assimilated information pertaining to the Angstrom exponent
585 will be highly beneficial, giving the model a sense of the aerosol speciation from the observations.

In its current form, GOCART-2G can reproduce observed aerosol properties but has some notable potential for
improvement. The spatial pattern of AOD across the globe is generally captured and the magnitude and seasonal cycle of AOD
agrees well with MODIS satellite observations. ~~Conversely, The general exceptions are that~~ regions characterized by dust ~~tend~~
~~to overestimate AOD and regions characterized by~~ ~~or~~ biomass burning aerosols ~~have overestimated and underestimated~~
590 ~~AOD tend to underestimate AOD, respectively~~. Further evaluation of surface aerosol mass in the United States suggests the
mass extinction efficiency for biomass burning aerosol is too low in GOCART-2G. This is corroborated by evaluations of
GEOS with GOCART-2G using data collected from recent airborne field campaigns (Collow et al., 2022). ~~An additional~~
~~concern elucidated by comparing the seasonal cycle of AOD over North America with the seasonal cycle of surface mass is~~
~~the loading of nitrate as both are overestimated in the winter and underestimated in the summer. Nitrate loading is likely only~~
595 ~~part of the reasoning behind the AOD bias as nitrate is minor contributor to the total aerosol. Nevertheless, the seasonal cycle~~
~~of nitrate, controlled by the prescribed oxidant fields from the MERRA-2 GMI simulation, should be further evaluated.~~
~~Finally, the modelled surface mass concentration of dust is biased low during the summer months across the United States,~~
~~coinciding with the underestimate in AOD. GOCART-2G is likely missing local sources of agricultural dust in the United~~
~~States.~~

600 ~~The concerns regarding the seasonal cycle of the AOD bias over Europe are more complicated. The EMEP database~~
~~did not include surface observations of dust for the time period of our benchmark simulation. On occasion, African dust is~~
~~transported northward into Europe with the occurrence of dust atmospheric rivers peaking in the spring months (Chakraborty~~
~~et al., 2022), and this is a feature that was not sufficiently evaluated here. Should dust in the model be deposited to quickly and~~

not reach central Europe, a negative bias in AOD would occur. Another possibility for the summertime AOD bias in GOCART2G is a deficiency in the aerosol extinction from long-range transported smoke from boreal wildfires. As was the case with the 2017 pyroCB events in British Columbia, wildfire smoke was lofted high enough such that it could circumnavigate the northern hemisphere and cause aerosol extinction to occur in the stratosphere over Europe. Das et al. (2022) demonstrated the GEOS modelled aerosol extinction in Germany was underestimated within the smoke plume that was transported from a pPyroCB event in British Columbia. In a situation such as this, the total column AOD would be impacted by the upper-level smoke however not corroborated by an increase in the concentration of surface particulate matter. Furthermore, we only included select pPyroCB events which means there could be additional cases in which smoke from Canada reaches Europe that are not represented in the model because the aerosol was emitted too low in altitude and deposited before crossing the Atlantic Ocean. Finally, the seasonal cycle of surface nitrate is amplified compared to observations.

Prescribed anthropogenic emissions are a source of uncertainty in the GEOS-GOCART2G modelled AOD and surface mass concentrations, particularly for regions such as North America, Europe, and Southern Asia. Emissions of SO₂ over China, India, Western Europe and the United States from the CEDS inventory are in general lower than the 2022 release version 6 of the Emissions Database for Global Atmospheric Research (EDGAR version 6) and the recent estimates from the Copernicus Atmosphere Monitoring Service (Soulie et al, 2023). The spread between the different emissions data products is particularly large over Asia. -Moreover, these data products provide monthly estimates that the GEOS-GOCART2G model linearly interpolates to a daily timescale. When doing so, the model does not impose a scaling based on the day of the week or the time of day, which could be an important indicator of the emissions on a sub-monthly timescale.

Based on the analysis presented here and results from previous studies found in literature, priorities for future development within GOCART-2G should include:

- Implementing a more physically based emission scheme and size distribution for dust to ~~easere~~reduce the overestimate in AOD over North Africa and improve the long-range transport of dust
- Increasing the mass extinction efficiency for biomass burning aerosol to decrease the overestimate in particulate matter while increasing the AOD in biomass burning regions
- Adjust vertical transport of biomass burning aerosol to represent self-lofting above the boundary layer
- Improve the assumptions of initial vertical placement of smoke from biomass burning sources to improve agreements with lidar observations
- Quantifying the uncertainty in AOD and surface particulate matter due to anthropogenic emissions and how this may change with a scaling factor for the day of the week or time of day
- Investigating the seasonal cycle of nitrate and precursor gaseous species that lead to the production of nitrate aerosol.
- Develop from the full chemistry simulations a simplified parameterization of the stratospheric sulphate aerosol.

Although this evaluation was comprehensive in terms of aerosol optical depth, surface mass, and the vertical profile of attenuated backscatter, the sources and sinks of individual aerosol species were not thoroughly evaluated and warrant future study.

640 ~~Though not discussed here, there are additional features of GOCART-2G that would benefit from future development. Bian et al. (2019) demonstrated a discrepancy in the particle size distribution for sea salt between GEOS and Particle Analysis by Laser Mass Spectrometry (PALMS) observations collected during the NASA ATom campaign. Although the largest two size bins for sea salt in GEOS were too coarse to be observed, it was evident that the model underestimated fine mode sea salt in the first two size bins. There are multiple papers in the literature that evaluate dust. Yu et al. (2020) noted that GEOS underestimated emissions of dust from haboobs and did not loft dust high enough into the middle troposphere for sufficient transport, resulting in an underestimate of the dust AOD in the Caribbean during a substantial dust event in June 2020. It was also pointed out by Kramer et al. (2020) that transported dust is overabundant in the boundary layer and has a particle size that is too large. There is also room for improvement in aerosol transport. As an example, Das et al. (2017) showed the biomass burning plume over the southeast Atlantic descends much too rapidly. With the flexibility and user friendly refactored code implemented within GOCART-2G it is anticipated that aerosol model developers will be able to work together to progress GOCART such improvements can be seen within these features in future versions.~~

645
650

Code Availability

GEOS, including GOCART-2G, is a publicly available Earth System model with source code at <https://github.com/GEOS-ESM> and <https://doi.org/10.5281/zenodo.8059710>. The archived code includes software to set up and run the model, compute
655 AOD from MODIS Level 2 reflectances, and post process the model output.

Data Availability

All observational data used are from publicly available datasets. MODIS Level 2 reflectances are available from
660 http://dx.doi.org/10.5067/MODIS/MOD04_L2.006 for Terra and http://dx.doi.org/10.5067/MODIS/MYD04_L2.006 for Aqua, CALIOP data can be downloaded at https://doi.org/10.5067/CALIOP/CALIPSO/LID_L15-STANDARD-V1-00, AERONET observations can be downloaded at https://aeronet.gsfc.nasa.gov/cgi-bin/webtool_aod_v3, IMPROVE data can be downloaded from the Federal Land Manager Environmental Database at <http://views.cira.colostate.edu/fed/DataWizard/Default.aspx>, and EMEP data can be downloaded from EBAS at [https://ebas-](https://ebas-data.nilu.no/)
665 [data.nilu.no/](https://ebas-data.nilu.no/). Model data, in addition to the observational data used, is archived at <http://dx.doi.org/10.5281/zenodo.8212822>.

Author Contribution

AC, PC, and VB contributed to the visualization. PC, AdS, and RG contributed to the software and data curation. AC was responsible for original draft preparation and PC, AdS, VB, MC, HB, DK, SD, and VA contributed to review and editing.

Competing Interests

670 The authors declare that they have no conflict of interest.

Acknowledgements

This work was accomplished through computing resources from the NASA Center for Climate Simulation (NCCS). Elliot Sherman is acknowledged for his work in refactoring GOCART. The software infrastructure team at NASA's Global Modeling Assimilation was invaluable throughout the process of developing GOCART-2G. We wish to thank Tom Clune, Ben Auer, 675 Weiyuan Jiang, Matt Thompson, and Atanas Trayanov for their assistance, as well as Anton Darmanov for providing his expertise throughout the code refactoring. [Matthew Johnson was an undergraduate NASA summer intern who assisted with the implementation of the new SOA schemes.](#)

We thank the AERONET PIs and Co-Is, and their staff, for establishing and maintaining the 80 sites used in this investigation. 680

IMPROVE is a collaborative association of state, tribal, and federal agencies, and international partners. US Environmental Protection Agency is the primary funding source, with contracting and research support from the National Park Service. The Air Quality Group at the University of California, Davis is the central analytical laboratory, with ion analysis provided by Research Triangle Institute, and carbon analysis provided by Desert Research Institute.

685 References

- Balkanski, Y. J., Jacob, D. J., Gardner, G. M., Graustein, W. C., and Turekian, K. K.: Transport and residence times of tropospheric aerosols inferred from a global three-dimensional simulation of 210Pb, *J. Geophys. Res.*, 98, 20573, <https://doi.org/10.1029/93JD02456>, 1993.
- 690 Bian, H., Chin, M., Hauglustaine, D. A., Schulz, M., Myhre, G., Bauer, S. E., Lund, M. T., Karydis, V. A., Kucsera, T. L., Pan, X., Pozzer, A., Skeie, R. B., Steenrod, S. D., Sudo, K., Tsigaridis, K., Tsimpidi, A. P., and Tsyro, S. G.: Investigation of global particulate nitrate from the AeroCom phase III experiment, *Atmos. Chem. Phys.*, 17, 12911–12940, <https://doi.org/10.5194/acp-17-12911-2017>, 2017.

695 Bian, H., Froyd, K., Murphy, D. M., Dibb, J., Darmenov, A., Chin, M., Colarco, P. R., da Silva, A., Kucsera, T. L., Schill, G.,
Yu, H., Bui, P., Dollner, M., Weinzierl, B., and Smirnov, A.: Observationally constrained analysis of sea salt aerosol in the
marine atmosphere, *Atmos. Chem. Phys.*, 19, 10773–10785, <https://doi.org/10.5194/acp-19-10773-2019>, 2019.

Bouwman, A. F., Lee, D. S., Asman, W. A. H., Dentener, F. J., Van Der Hoek, K. W., and Olivier, J. G. J.: A global high-
700 resolution emission inventory for ammonia, *Global Biogeochem. Cy.*, 11, 561–587, <https://doi.org/10.1029/97GB02266>, 1997.

Bozzo, A., Benedetti, A., Flemming, J., Kipling, Z., and Rémy, S.: An aerosol climatology for global models based on the
tropospheric aerosol scheme in the Integrated Forecasting System of ECMWF, *Geosci. Model Dev.*, 13, 1007–1034,
<https://doi.org/10.5194/gmd-13-1007-2020>, 2020.

705

Buchard, V., Da Silva, A. M., Randles, C. A., Colarco, P., Ferrare, R., Hair, J., Hostetler, C., Tackett, J and Winker, D.:
Evaluation of the surface PM_{2.5} in Version 1 of the NASA MERRA Aerosol Reanalysis over the United States. *Atmospheric
Environment*, 125, 100-111, <https://doi.org/10.1016/j.atmosenv.2015.11.004>, 2016.

710 Buchard, V., Randles, C. A., da Silva, A. M., Darmenov, A., Colarco, P. R., Govindaraju, R., Ferrare, R., Hair, J., Beyersdorf,
A. J., Ziemba, L. D., and Yu, H: The MERRA-2 Aerosol Reanalysis, 1980 Onward. Part II: Evaluation and Case Studies.
Journal of Climate 30, 17, 6851-6872, <https://doi.org/10.1175/JCLI-D-16-0613.1>, 2017.

Burgos, M. A., Andrews, E., Titos, G., Benedetti, A., Bian, H., Buchard, V., Curci, G., Kipling, Z., Kirkevåg, A., Kokkola,
715 H., Laakso, A., Letertre-Danczak, J., Lund, M. T., Matsui, H., Myhre, G., Randles, C., Schulz, M., van Noije, T., Zhang, K.,
Alados-Arboledas, L., Baltensperger, U., Jefferson, A., Sherman, J., Sun, J., Weingartner, E., and Zieger, P.: A global model-
measurement evaluation of particle light scattering coefficients at elevated relative humidity, *Atmos. Chem. Phys.*, 20, 10231–
10258, <https://doi.org/10.5194/acp-20-10231-2020>, 2020.

720 Carn, S. A., Fioletov, V. E., McLinden, C. A., Li, C., and Krotkov, N. A.: A decade of global volcanic SO₂ emissions measured
from space, *Sci. Rep.*, 7, 44095, <https://doi.org/10.1038/srep44095>, 2017.

[Case, P., Colarco, P. R., Toon, B., Aquila, V., & Keller, C. A.: Interactive stratospheric aerosol microphysics-chemistry
simulations of the 1991 Pinatubo volcanic aerosols with newly coupled sectional aerosol and stratosphere-troposphere
725 chemistry modules in the NASA GEOS Chemistry-Climate Model \(CCM\). *Journal of Advances in Modeling Earth Systems*,
15, e2022MS003147, <https://doi.org/10.1029/2022MS003147>, 2023.](#)

[Chakraborty, S., Guan, B., Waliser, D. E., and da Silva, A. M.: Aerosol atmospheric rivers: climatology, event characteristics, and detection algorithm sensitivities, Atmos. Chem. Phys., 22, 8175–8195, https://doi.org/10.5194/acp-22-8175-2022, 2022.](https://doi.org/10.5194/acp-22-8175-2022)

730

Chin, M., Rood, R. B., Lin, S.-J., Müller, J.-F., and Thompson, A. M.: Atmospheric sulfur cycle simulated in the global model GOCART: Model description and global properties, *J. Geophys. Res.-Atmos.*, 105, 24671–24687, <https://doi.org/10.1029/2000JD900384>, 2000.

735 Chin, M., Ginoux, P., Kinne, S., Torres, O., Holben, B. N., Duncan, B. N., Martin, R. V., Logan, J. A., Higurashi, A., and Nakajima, T.: Tropospheric aerosol optical thickness from the GOCART model and comparisons with satellite and sun photometer measurements, *J. Atmos. Sci.*, 59, 461–483, [https://doi.org/10.1175/1520-0469\(2002\)059<0461:taotft>2.0.co;2](https://doi.org/10.1175/1520-0469(2002)059<0461:taotft>2.0.co;2), 2002.

740 Chin, M., Chu, A., Levy, R., Remer, L., Kaufman, Y., Holben, B., Eck, T., Ginoux, P., and Gao, Q.: Aerosol distribution in the Northern Hemisphere during ACE-Asia: Results from global model, satellite observations, and Sun photometer measurements, *J. Geophys. Res.-Atmos.*, 109, 1–15, <https://doi.org/10.1029/2004JD004829>, 2004.

Clough, S.A., Shephard, M.W., Mlawer, E.J., Delamere, J.S., Iacono, M.J., Cady-Pereira, K., Boukabara, S. and Brown, P.D.:
745 Atmospheric radiative transfer modeling: a summary of the AER codes, *J. Quant. Spectrosc. Radiat. Transfer*, 91, 233-244, 2005.

Colarco, P., Da Silva, A., Chin, M., and Diehl, T.: Online simulations of global aerosol distributions in the NASA GEOS-4 model and comparisons to satellite and ground-based aerosol optical depth, *J. Geophys. Res.-Atmos.*, 115, D14207,
750 <https://doi.org/10.1029/2009JD012820>, 2010.

Colarco, P. R., Nowottnick, E. P., Randles, C. A., Yi, B., Yang, P., Kim, K.-M., Smith, J. A., and Bardeen, C. G.: Impact of radiatively interactive dust aerosols in the NASA GEOS-5 climate model: Sensitivity to dust particle shape and refractive index, *J. Geophys. Res.-Atmos.*, 119, 753–786, <https://doi.org/10.1002/2013JD020046>, 2014.

755

Colarco, P. R., Gassó, S., Ahn, C., Buchard, V., da Silva, A. M., and Torres, O.: Simulation of the Ozone Monitoring Instrument aerosol index using the NASA Goddard Earth Observing System aerosol reanalysis products, *Atmos. Meas. Tech.*, 10, 4121–4134, <https://doi.org/10.5194/amt-10-4121-2017>, 2017.

760 Collow, A. B. M., Buchard, V., Colarco, P. R., da Silva, A. M., Govindaraju, R., Nowottnick, E. P., Burton, S., Ferrare, R., Hostetler, C., and Ziemba, L.: An evaluation of biomass burning aerosol mass, extinction, and size distribution in GEOS using observations from CAMP2Ex, *Atmos. Chem. Phys.*, 22, 16091–16109, <https://doi.org/10.5194/acp-22-16091-2022>, 2022.

Collow, A., Buchard, V., Chin, M., Colarco, P., Darmenov, A., and da Silva, A.: Supplemental Documentation for GEOS
765 Aerosol Products. GMAO Office Note No. 22 (Version 1.0), 8 pp, available from <https://gmao.gsfc.nasa.gov/pubs/docs/Collow1463.pdf> [accessed 9 March 2023], 2023.

Darmenov, A. and da Silva, A.: The quick fire emissions dataset (QFED) – Documentation of versions 2.1, 2.2 and 2.4. NASA//TM-2015-104606, Vol. 38, NASA Global Modeling and Assimilation Office, 183 pp., available at:
770 <https://gmao.gsfc.nasa.gov/pubs/docs/Darmenov796.pdf> [accessed 2 August 2022], 2015.

Das, S., Harshvardhan, H., Bian, H., Chin, M., Curci, G., Protonotariou, A.P., Mielonen, T., Zhang, K., Wang, H., and Liu, X.: Biomass burning aerosol transport and vertical distribution over the South African-Atlantic region, *J. Geophys. Res.-Atmos.*, 122, 6391–6415, <https://doi.org/10.1002/2016JD026421>, 2017.

775

Das, S., Colarco, P. R., Oman, L. D., Taha, G., and Torres, O.: The long-term transport and radiative impacts of the 2017 British Columbia pyrocumulonimbus smoke aerosols in the stratosphere, *Atmos. Chem. Phys.*, 21, 12069–12090, <https://doi.org/10.5194/acp-21-12069-2021>, 2021.

780 Gelaro, R., McCarty, W., Suarez, M. J., Todling, R., Molod, A., Takacs, L., Randles, C. A., Darmenov, A., Bosilovich, M. G., Reichle, R., Wargan, K., Coy, L., Cullather, R., Draper, C., Akella, S., Buchard, V., Conaty, A., Silva, A. M. da, Gu, W., Kim, G.-K., Koster, R., Lucchesi, R., Merkova, D., Nielsen, J. E., Partyka, G., Pawson, S., Putman, W., Rienecker, M., Schubert, S. D., Sienkiewicz, M., and Zhao, B.: The Modern-Era Retrospective Analysis for Research and Applications, Version 2 (MERRA-2), *J. Climate*, 30, 5419–5454, <https://doi.org/10.1175/JCLI-D-16-0758.1>, 2017.

785

Giles, D. M., Sinyuk, A., Sorokin, M. G., Schafer, J. S., Smirnov, A., Slutsker, I., Eck, T. F., Holben, B. N., Lewis, J. R., Campbell, J. R., Welton, E. J., Korkin, S. V., and Lyapustin, A. I.: Advancements in the Aerosol Robotic Network (AERONET) Version 3 database – automated near-real-time quality control algorithm with improved cloud screening for Sun photometer aerosol optical depth (AOD) measurements, *Atmos. Meas. Tech.*, 12, 169–209, <https://doi.org/10.5194/amt-12-169-2019>, 2019.

790

Giorgi, F. and Chameides, L. W.: Rainout lifetimes of highly soluble aerosols and gases as inferred from simulations with a general circulation model, *J. Geophys. Res.*, 91, 14367–14376, 1986.

795 Ginoux, P., Chin, M., Tegen, I., Prospero, J. M., Holben, B., Dubovik, O., and Lin, S.-J.: Sources and distributions of dust aerosols simulated with the GOCART model. *J. Geophys. Res.*, 106, 20 255–20 273, <https://doi.org/10.1029/2000JD000053>, 2001.

800 Gliß, J., Mortier, A., Schulz, M., Andrews, E., Balkanski, Y., Bauer, S. E., Benedictow, A. M. K., Bian, H., Checa-Garcia, R., Chin, M., Ginoux, P., Griesfeller, J. J., Heckel, A., Kipling, Z., Kirkevåg, A., Kokkola, H., Laj, P., Le Sager, P., Lund, M. T., Lund Myhre, C., Matsui, H., Myhre, G., Neubauer, D., van Noije, T., North, P., Olivić, D. J. L., Rémy, S., Sogacheva, L., Takemura, T., Tsigaridis, K., and Tsyro, S. G.: AeroCom phase III multi-model evaluation of the aerosol life cycle and optical properties using ground- and space-based remote sensing as well as surface in situ observations, *Atmos. Chem. Phys.*, 21, 87–128, <https://doi.org/10.5194/acp-21-87-2021>, 2021.

805 Gong, S. L.: A parameterization of sea-salt aerosol source function for sub- and super-micron particles. *Global Biogeochem. Cycles*, 17, 1097, <https://doi.org/10.1029/2003GB002079>, 2003.

Grell, G. A. and Freitas, S. R.: A scale and aerosol aware stochastic convective parameterization for weather and air quality
810 modeling, *Atmos. Chem. Phys.*, 14, 5233–5250, <https://doi.org/10.5194/acp-14-5233-2014>, 2014.

~~Guenther, A. B., Jiang, X., Heald, C. L., Sakulyanontvittaya, T., Duhl, T., Emmons, L. K., and Wang, X.: The Model of Emissions of Gases and Aerosols from Nature version 2.1 (MEGAN2.1): an extended and updated framework for modeling biogenic emissions, *Geosci. Model Dev.*, 5, 1471–1492, <https://doi.org/10.5194/gmd-5-1471-2012>.~~

815 Hand, J. L., Copeland, S. A., Day, D. R., Dillner, A. M., Indresand, H., Malm, W. C., McDade, C. E., Moore, C. T., Pitchford, M. L., Schichtel, B. A., and Watson, J. G.: Spatial and Seasonal Patterns and Temporal Variability of Haze and its Constituents in the United States Report V, http://vista.cira.colostate.edu/Improve/wp-content/uploads/2016/04/Cover_TOC.pdf [accessed 24 August 2022], 2011.

820 Hess, M., Koepke, P., and Schult, I.: Optical properties of aerosols and clouds: The software package OPAC, *B. Am. Meteorol. Soc.*, 79, 831–844, [https://doi.org/10.1175/1520-0477\(1998\)079<0831:OPOAAC>2.0.CO;2](https://doi.org/10.1175/1520-0477(1998)079<0831:OPOAAC>2.0.CO;2), 1998.

~~Hodzic, A. and Jimenez, J. L.: Modeling anthropogenically controlled secondary organic aerosols in a megacity: a simplified framework for global and climate models, *Geosci. Model Dev.*, 4, 901–917, <https://doi.org/10.5194/gmd-4-901-2011>.~~

825

Hodzic, A., Campuzano-Jost, P., Bian, H., Chin, M., Colarco, P. R., Day, D. A., Froyd, K. D., Heinold, B., Jo, D. S., Katich, J. M., Kodros, J. K., Nault, B. A., Pierce, J. R., Ray, E., Schacht, J., Schill, G. P., Schroder, J. C., Schwarz, J. P., Sueper, D. T., Tegen, I., Tilmes, S., Tsigaridis, K., Yu, P., and Jimenez, J. L.: Characterization of organic aerosol across the global remote troposphere: a comparison of ATom measurements and global chemistry models, *Atmos. Chem. Phys.*, 20, 4607–4635, <https://doi.org/10.5194/acp-20-4607-2020>, 2020.

Hoesly, R. M., Smith, S. J., Feng, L., Klimont, Z., Janssens-Maenhout, G., Pitkanen, T., Seibert, J. J., Vu, L., Andres, R. J., Bolt, R. M., Bond, T. C., Dawidowski, L., Kholod, N., Kurokawa, J.-I., Li, M., Liu, L., Lu, Z., Moura, M. C. P., O'Rourke, P. R., and Zhang, Q.: Historical (1750–2014) anthropogenic emissions of reactive gases and aerosols from the Community Emissions Data System (CEDS), *Geosci. Model Dev.*, 11, 369–408, <https://doi.org/10.5194/gmd-11-369-2018>, 2018.

Holben, B. N., Eck, T. F., Slutsker, I., Tanre, D., Buis, J. P., Setzer, A., Vermote, E., Reagan, J. A., Kaufman, Y., Nakajima, T., Lavenue, F., Jankowiak, I., and Smirnov, A.: AERONET – A federated instrument network and data archive for aerosol characterization, *Remote Sens. Environ.*, 66, 1–16, [https://doi.org/10.1016/S0034-4257\(98\)00031-5](https://doi.org/10.1016/S0034-4257(98)00031-5), 1998.

Iacono, M.J., Delamere, J.S., Mlawer, E.J., Shephard, M.W., Clough, S.A., and Collins, W.D.: Radiative forcing by long-lived greenhouse gases: Calculations with the AER radiative transfer models, *J. Geophys. Res.*, 113, D13103, doi:10.1029/2008JD009944, 2008.

Jaeglé, L., Quinn, P. K., Bates, T. S., Alexander, B., and Lin, J.-T.: Global distribution of sea salt aerosols: new constraints from in situ and remote sensing observations, *Atmos. Chem. Phys.*, 11, 3137–3157, <https://doi.org/10.5194/acp-11-3137-2011>, 2011.

~~Keller, C. A., Long, M. S., Yantosea, R. M., Da Silva, A. M., Pawson, S., and Jacob, D. J.: HEMCO v1.0: a versatile, ESMF-compliant component for calculating emissions in atmospheric models, *Geosci. Model Dev.*, 7, 1409–1417, <https://doi.org/10.5194/gmd-7-1409-2014>.~~

Kemppinen, O., Colarco, P.R., and Castellanos, P.: GEOS aerosol optical table calculation package GEOSmie, NASA Technical Report Series on Global Modeling and Data Assimilation, Volume 63, <https://gmao.gsfc.nasa.gov/pubs/docs/Kemppinen1447.pdf> [accessed 13 January 2023], 2022.

~~Kim, P. S., Jacob, D. J., Fisher, J. A., Travis, K., Yu, K., Zhu, L., Yantosea, R. M., Sulprizio, M. P., Jimenez, J. L., Campuzano-Jost, P., Froyd, K. D., Liao, J., Hair, J. W., Fenn, M. A., Butler, C. F., Wagner, N. L., Gordon, T. D., Welti, A., Wennberg, P. O., Crounse, J. D., Clair, J. M. S., Teng, A. P., Millet, D. B., Schwarz, J. P., Markovic, M. Z., and Perring, A. E.: Sources,~~

~~seasonality, and trends of southeast US aerosol: an integrated analysis of surface, aircraft, and satellite observations with the GEOS-Chem chemical transport model, Atmos Chem Phys, 15, 10411–10433, <https://doi.org/10.5194/acp-15-10411-2015>, 2015.~~

865 [Kim, D., Chin, M., Yu, H., Diehl, T., Tan, Q., Kahn, R. A., Tsigaridis, K., Bauer, S. E., Takemura, T., Pozzoli, L., Bellouin, N., Schulz, M., Peyridieu, S., Chédin, A., and Koffi, B.: Sources, sinks, and transatlantic transport of North African dust aerosol: A multimodel analysis and comparison with remote sensing data, J. Geophys. Res.-Atmos., 119, 6259–6277, <https://doi.org/10.1002/2013JD021099>, 2014.](#)

870 [Kim, D., Chin, M., Yu, H., Pan, X., Bian, H., Tan, Q., Kahn, R. A., Tsigaridis, K., Bauer, S. E., Takemura, T., Pozzoli, L., Bellouin, N., and Schulz, M.: Asian and Trans-Pacific Dust: A Multimodel and Multiremote Sensing Observation Analysis, J. Geophys. Res.-Atmos., 124, 13534–13559, <https://doi.org/10.1029/2019JD030822>, 2019.](#)

Kim, D., Chin, M., Cruz, C. A., Tong, D., & Yu, H.: ~~(2021)~~ Spring dust in western North America and its interannual
875 variability—Understanding the role of local and transported dust. Journal of Geophysical Research: Atmospheres, 126, e2021JD035383. <https://doi.org/10.1029/2021JD035383>, 2021.

[Kok, J. F., Adebisi, A. A., Albani, S., Balkanski, Y., Checa-Garcia, R., Chin, M., Colarco, P. R., Hamilton, D. S., Huang, Y., Ito, A., Klose, M., Leung, D. M., Li, L., Mahowald, N. M., Miller, R. L., Obiso, V., Pérez García-Pando, C., Rocha-Lima, A.,
880 Wan, J. S., and Whicker, C. A.: Improved representation of the global dust cycle using observational constraints on dust properties and abundance, Atmos. Chem. Phys., 21, 8127–8167, <https://doi.org/10.5194/acp-21-8127-2021>, 2021.](#)

~~Kim, D., Chin, M., Yu, H., Pan, X., Bian, H., Tan, Q., Kahn, R. A., Tsigaridis, K., Bauer, S. E., Takemura, T., Pozzoli, L.,
Bellouin, N., and Schulz, M.: Asian and Trans-Pacific Dust: A Multimodel and Multiremote Sensing Observation Analysis, J.
885 Geophys. Res. Atmos., 124, 13534–13559, <https://doi.org/10.1029/2019JD030822>, 2019.~~

Kramer, S. J., Alvarez, C., Barkley, A. E., Colarco, P. R., Custals, L., Delgado, R., Gaston, C. J., Govindaraju, R., and Zuidema, P.: Apparent dust size discrepancy in aerosol reanalysis in north African dust after long-range transport, Atmos. Chem. Phys., 20, 10047–10062, <https://doi.org/10.5194/acp-20-10047-2020>, 2020.

890

Lana, A., Bell, T. G., Simó, R., Vallina, S. M., Ballabrera-Poy, J., Kettle, A. J., Dachs, J., Bopp, L., Saltzman, E. S., Stefels, J., Johnson, J. E., and Liss, P. S.: An updated climatology of surface dimethylsulfide concentrations and emission fluxes in the global ocean, Global Biogeochem. Cy., 25, GB1004 <https://doi.org/10.1029/2010GB003850>, 2011.

- 895 Levy, R., Hsu, C., et al.: MODIS Atmosphere L2 Aerosol Product. NASA MODIS Adaptive Processing System, Goddard Space Flight Center, USA, http://dx.doi.org/10.5067/MODIS/MYD04_L2.061, 2015.
- Liss, P. S. and Merlivat, L.: Air-sea gas exchange rates: Introduction and synthesis, in: *The Role of Air-Sea Exchange in Geochemical Cycling*, edited by: Buat-Menard, P., Dreidel, Norwell, Mass., 113–127, 1986.
- 900 Liu, H., Jacob, D., Bey, I., and Yantosca, R.: Constraints from Pb-210 and Be-7 on wet deposition and transport in a global three-dimensional chemical tracer model driven by assimilated meteorological fields, 106, <https://doi.org/10.1029/2000JD900839>, 2001.
- 905 Liu, X., Ma, P.-L., Wang, H., Tilmes, S., Singh, B., Easter, R. C., Ghan, S. J., and Rasch, P. J.: Description and evaluation of a new four-mode version of the Modal Aerosol Module (MAM4) within version 5.3 of the Community Atmosphere Model, *Geosci. Model Dev.*, 9, 505–522, <https://doi.org/10.5194/gmd-9-505-2016>, 2016.
- Lock, A. P., Brown, A. R., Bush, M. R., Martin, G. M., and Smith, R. N. B.: A New Boundary Layer Mixing Scheme. Part I: Scheme Description and Single-Column Model Tests, *Mon. Weather Rev.*, 128, 3187–3199, [https://doi.org/10.1175/1520-0493\(2000\)128<3187:ANBLMS>2.0.CO;2](https://doi.org/10.1175/1520-0493(2000)128<3187:ANBLMS>2.0.CO;2), 2000.
- Louis, JF.: A parametric model of vertical eddy fluxes in the atmosphere. *Boundary-Layer Meteorol.* 17, 187–202, <https://doi.org/10.1007/BF00117978>, 1979.
- 915 Lu, C.-H., da Silva, A., Wang, J., Moorthi, S., Chin, M., Colarco, P., Tang, Y., Bhattacharjee, P. S., Chen, S.-P., Chuang, H.-Y., Juang, H.-M. H., McQueen, J., and Iredell, M.: The implementation of NEMS GFS Aerosol Component (NGAC) Version 1.0 for global dust forecasting at NOAA/NCEP, *Geosci. Model Dev.*, 9, 1905–1919, <https://doi.org/10.5194/gmd-9-1905-2016>, 2016.
- 920 Lucchesi, R.: File Specification for GEOS FP. GMAO Office Note No. 4 (Version 1.2), 61 pp, available from http://gmao.gsfc.nasa.gov/pubs/office_notes [accessed 9 March 2023], 2018.
- Maria, S. F., Russell, L. M., Gilles, M. K., and Myneni, S. C. B.: Organic aerosol growth mechanisms and their climate-forcing implications, *Science*, 306, 1921–1924, <https://doi.org/10.1126/science.1103491>, 2004.

[McDuffie, E. E., Smith, S. J., O'Rourke, P., Tibrewal, K., Venkataraman, C., Marais, E. A., Zheng, B., Crippa, M., Brauer, M., and Martin, R. V.: A global anthropogenic emission inventory of atmospheric pollutants from sector- and fuel-specific](#)

- sources (1970–2017): an application of the Community Emissions Data System (CEDS), *Earth Syst. Sci. Data*, 12, 3413–3442, <https://doi.org/10.5194/essd-12-3413-2020>, 2020.
- 930
- Molod, A., Hackert, E., Vikhliayev, Y., Zhao, B., Barahona, D., Vernieres, G., Borovikov, A., Kovach, R. M., Marshak, J., Schubert, S., Li, Z., Lim, Y.-K., Andrews, L. C., Cullather, R., Koster, R., Achuthavarier, D., Carton, J., Coy, L., Friere, J. L. M., Longo, K. M., Nakada, K., and Pawson, S.: GEOS-S2S Version 2: The GMAO High-Resolution Coupled Model and
935 Assimilation System for Seasonal Prediction, *J. Geophys. Res.-Atmos.*, 125, e2019JD031767, <https://doi.org/10.1029/2019JD031767>, 2020.
- NASA/LARC/SD/ASDC. CALIPSO Lidar Level 1.5 Profile, V1-00. NASA Langley Atmospheric Science Data Center DAAC; 2019. Available from: https://doi.org/10.5067/CALIOP/CALIPSO/LID_L15-STANDARD-V1-00
940
- Nielsen, J., Pawson, S., Molod, A., Auer, B., da Silva, A., Douglass, A., Duncan, B., Liang, Q., Manyin, M., Oman, L., Putman, W., Strahan, S., and Wargan, K.: Chemical Mechanisms and Their Applications in the Goddard Earth Observing System (GEOS) Earth System Model, *J. Adv. Model. Earth Syst.*, 9, 3019–3044, <https://doi.org/10.1002/2017MS001011>, 2017.
- 945 Pan, X., Ichoku, C., Chin, M., Bian, H., Darmenov, A., Colarco, P., Ellison, L., Kucsera, T., da Silva, A., Wang, J., Oda, T., and Cui, G.: Six global biomass burning emission datasets: intercomparison and application in one global aerosol model, *Atmos. Chem. Phys.*, 20, 969–994, <https://doi.org/10.5194/acp-20-969-2020>, 2020.
- Provençal, S., Buchard, V., da Silva, A.M., Leduc, R., and Barrette, N.: Evaluation of PM surface concentrations simulated by
950 Version 1 of NASA's MERRA Aerosol Reanalysis over Europe, *Atmos Pollut Res.*, 8(2), 374-382, <https://doi.org/10.1016/j.apr.2016.10.009>, 2017.
- Randles, C. A., da Silva, A.M., Buchard, V., Darmenov, A., Colarco, P.R., Aquila, V., Bian, H., Nowottnick, E.P., Pan, X., Smirnov, A. Yu, H. and R. Govindaraju, R.: The MERRA-2 Aerosol Assimilation. NASA Technical Report Series on Global
955 Modeling and Data Assimilation, NASA/TM-2016-104606, Vol. 45, 143 pp, <https://gmao.gsfc.nasa.gov/pubs/docs/Randles887.pdf> [accessed 7 March 2023], 2016.
- Randles, C. A., da Silva, A. M., Buchard, V., Colarco, P. R., Darmenov, A., Govindaraju, R., Smirnov, A., Holben, B., Ferrare, R., Hair, J., Shinozuka, Y., and Flynn, C. J.: The MERRA-2 Aerosol Reanalysis, 1980 Onward. Part I: System Description
960 and Data Assimilation Evaluation, *Journal of Climate*, 30(17), 6823-6850, <https://doi.org/10.1175/JCLI-D-16-0609.1>, 2017.

Remer, L. A., Levy, R. C., Mattoo, S., Tanré, D., Gupta, P., Shi, Y., Sawyer, V., Munchak, L. A., Zhou, Y., Kim, M., Ichoku, C., Patadia, F., Li, R.-R., Gassó, S., Kleidman, R. G., and Holben, B. N.: The Dark Target Algorithm for Observing the Global Aerosol System: Past, Present, and Future, *Remote Sens.*, 12, 2900, <https://doi.org/10.3390/rs12182900>, 2020.

965

Rémy, S., Kipling, Z., Flemming, J., Boucher, O., Nabat, P., Michou, M., Bozzo, A., Ades, M., Huijnen, V., Benedetti, A., Engelen, R., Peuch, V.-H., and Morcrette, J.-J.: Description and evaluation of the tropospheric aerosol scheme in the European Centre for Medium-Range Weather Forecasts (ECMWF) Integrated Forecasting System (IFS-AER, cycle 45R1), *Geosci. Model Dev.*, 12, 4627–4659, <https://doi.org/10.5194/gmd-12-4627-2019>, 2019.

970

Reynolds, R. W., Rayner, N. A., Smith, T. M., Stokes, D. C., and Wang, W.: An Improved In Situ and Satellite SST Analysis for Climate. *Journal of Climate* 15, 13, 1609-1625, [https://doi.org/10.1175/1520-0442\(2002\)015<1609:AIISAS>2.0.CO;2](https://doi.org/10.1175/1520-0442(2002)015<1609:AIISAS>2.0.CO;2), 2002.

975

~~Sander, S. P., J. Abbatt, J. R. Barker, J. B. Burkholder, R. R. Friedl, D. M. Golden, R. E. Huie, C. E. Kolb, M. J. Kurylo, G. K. Moortgat, V. L. Orkin and P. H. Wine "Chemical Kinetics and Photochemical Data for Use in Atmospheric Studies, Evaluation No. 17," JPL Publication 10-6, Jet Propulsion Laboratory, Pasadena, 2011 <http://jpldataeval.jpl.nasa.gov>.~~

980

Saxena, P., Hudischewskyj, A. B., Seigneur, C., and Seinfeld, J. H.: A comparative study of equilibrium approaches to the chemical characterization of secondary aerosols, *Atmos. Environ.*, 20, 1471–1483, [https://doi.org/10.1016/0004-6981\(86\)90019-3](https://doi.org/10.1016/0004-6981(86)90019-3), 1986.

985

Sayer, A. M., Hsu, N. C., Lee, J., Kim, W. V., and Dutcher, S. T.: Validation, Stability, and Consistency of MODIS Collection 6.1 and VIIRS Version 1 Deep Blue Aerosol Data Over Land, *J. Geophys. Res.-Atmos.*, 124, 4658–4688, <https://doi.org/10.1029/2018JD029598>, 2019.

990

Schwartz, M. J., Pumphrey, H. C., Santee, M. L., Manney, G. L., Lambert, A., Livesey, N. J., Millán, L., Neu, J. L., Read, W. J., and Werner, F.: Australian New Year's PyroCb impact on Stratospheric Composition, *Geophys. Res. Lett.*, 47, e2020GL090831, <https://doi.org/10.1029/2020GL090831>, 2020.

995

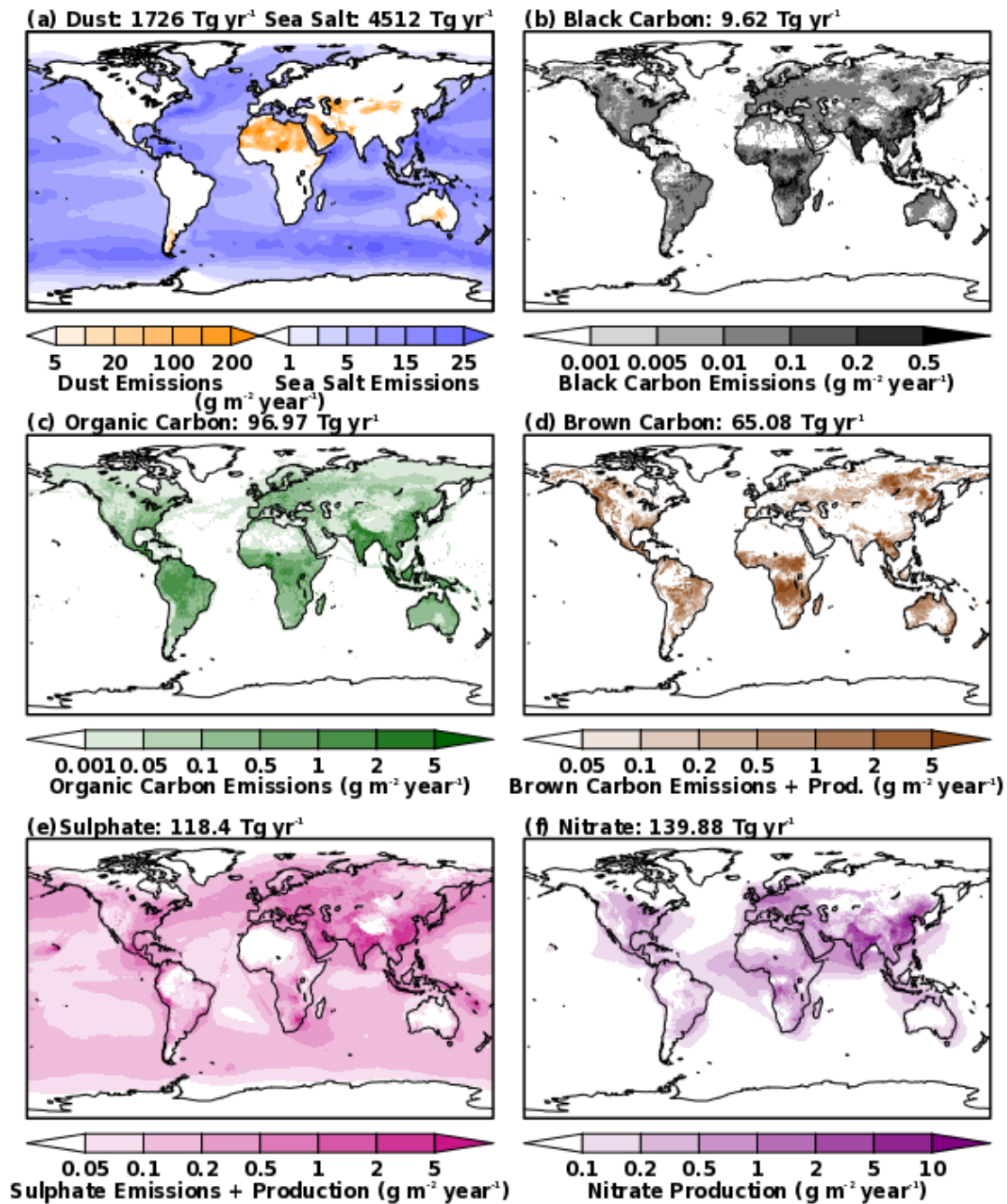
[Soulie, A., Granier, C., Darras, S., Zilbermann, N., Doumbia, T., Guevara, M., Jalkanen, J.-P., Keita, S., Lioussé, C., Crippa, M., Guizzardi, D., Hoesly, R., and Smith, S.: Global Anthropogenic Emissions \(CAMSGLOBANT\) for the Copernicus Atmosphere Monitoring Service Simulations of Air Quality Forecasts and Reanalyses, *Earth Syst. Sci. Data Discuss.* \[preprint\], <https://doi.org/10.5194/essd-2023-306>, in review, 2023.](https://doi.org/10.5194/essd-2023-306)

- Strode, S. A., Ziemke, J. R., Oman, L. D., Lamsal, L. N., Olsen, M. A., and Liu, J.: Global changes in the diurnal cycle of surface ozone, *Atmos. Environ.*, 199, 323–333, <https://doi.org/10.1016/j.atmosenv.2018.11.028>, 2019.
- Taha, G., Loughman, R., Zhu, T., Thomason, L., Kar, J., Rieger, L., and Bourassa, A.: OMPS LP Version 2.0 multi-wavelength aerosol extinction coefficient retrieval algorithm, *Atmos. Meas. Tech.*, 14, 1015–1036, <https://doi.org/10.5194/amt-14-1015-2021>, 2021.
- Tegen, I. and Lacis, A. A.: Modeling of particle size distribution and its influence on the radiative properties of mineral dust aerosol, *J. Geophys. Res.-Atmos.*, 101, 19237–19244, <https://doi.org/10.1029/95jd03610>, 1996.
- Textor, C., Schulz, M., Guibert, S., Kinne, S., Balkanski, Y., Bauer, S., Berntsen, T., Berglen, T., Boucher, O., Chin, M., Dentener, F., Diehl, T., Easter, R., Feichter, H., Fillmore, D., Ghan, S., Ginoux, P., Gong, S., Grini, A., Hendricks, J., Horowitz, L., Huang, P., Isaksen, I., Iversen, I., Kloster, S., Koch, D., Kirkevåg, A., Kristjansson, J. E., Krol, M., Lauer, A., Lamarque, J. F., Liu, X., Montanaro, V., Myhre, G., Penner, J., Pitari, G., Reddy, S., Seland, Ø., Stier, P., Takemura, T., and Tie, X.: Analysis and quantification of the diversities of aerosol life cycles within AeroCom, *Atmos. Chem. Phys.*, 6, 1777–1813, <https://doi.org/10.5194/acp-6-1777-2006>, 2006.
- Torres, O., Bhartia, P. K., Taha, G., Jethva, H., Das, S., Colarco, P., Krotkov, N., Omar, A., and Ahn, C.: Stratospheric Injection of Massive Smoke Plume From Canadian Boreal Fires in 2017 as Seen by DSCOVR-EPIC, CALIOP, and OMPS-LP Observations, *J. Geophys. Res.-Atmos.*, 125, D032579, <https://doi.org/10.1029/2020JD032579>, 2020.
- Tsigaridis, K., Daskalakis, N., Kanakidou, M., Adams, P. J., Artaxo, P., Bahadur, R., Balkanski, Y., Bauer, S. E., Bellouin, N., Benedetti, A., Bergman, T., Berntsen, T. K., Beukes, J. P., Bian, H., Carslaw, K. S., Chin, M., Curci, G., Diehl, T., Easter, R. C., Ghan, S. J., Gong, S. L., Hodzic, A., Hoyle, C. R., Iversen, T., Jathar, S., Jimenez, J. L., Kaiser, J. W., Kirkevåg, A., Koch, D., Kokkola, H., Lee, Y. H., Lin, G., Liu, X., Luo, G., Ma, X., Mann, G. W., Mihalopoulos, N., Morcrette, J.-J., Müller, J.-F., Myhre, G., Myriokefalitakis, S., Ng, N. L., O'Donnell, D., Penner, J. E., Pozzoli, L., Pringle, K. J., Russell, L. M., Schulz, M., Sciare, J., Seland, Ø., Shindell, D. T., Sillman, S., Skeie, R. B., Spracklen, D., Stavrou, T., Steenrod, S. D., Takemura, T., Tiitta, P., Tilmes, S., Tost, H., van Noije, T., van Zyl, P. G., von Salzen, K., Yu, F., Wang, Z., Wang, Z., Zaveri, R. A., Zhang, H., Zhang, K., Zhang, Q., and Zhang, X.: The AeroCom evaluation and intercomparison of organic aerosol in global models, *Atmos. Chem. Phys.*, 14, 10845–10895, <https://doi.org/10.5194/acp-14-10845-2014>, 2014.
- Wesely, M. L.: Parameterization of Surface Resistances to Gaseous Dry Deposition in Regional-Scale Numerical-Models, *Atmos. Environ.*, 23, 1293–1304, [https://doi.org/10.1016/0004-6981\(89\)90153-4](https://doi.org/10.1016/0004-6981(89)90153-4), 1989.

- 1030 Winker, D. M., W. H. Hunt, and M. J. McGill: Initial performance assessment of CALIOP. *Geophys. Res. Lett.*, L19803, doi:10.1029/2007GL030135, 2007.
- Winker, D. M., M. A. Vaughan, A. Omar, Y. Hu, K. A. Powell, Z. Liu, W. H. Hunt, and S. A. Young: Overview of the CALIPSO mission and CALIOP data processing algorithms. *J. Atmos. Oceanic Technol.*, 26, 2310–2323, 1035 doi:10.1175/2009JTECHA1281., 2009.
- Xian, P., Reid, J. S., Hyer, E. J., Sampson, C. R., Rubin, J. I., Ades, M., Asencio, N., Basart, S., Benedetti, A., Bhattacharjee, P. S., Brooks, M. E., Colarco, P. R., da Silva, A. M., Eck, T. F., Guth, J., Jorba, O., Kouznetsov, R., Kipling, Z., Sofiev, M., Perez Garcia-Pando, C., Pradhan, Y., Tanaka, T., Wang, J., Westphal, D. L., Yumimoto, K., and Zhang, J.: Current state of 1040 the global operational aerosol multi-model ensemble: An update from the International Cooperative for Aerosol Prediction (ICAP), *Q. J. Roy. Meteor. Soc.*, 145, 176–209, <https://doi.org/10.1002/qj.3497>, 2019.
- Yu, P., Toon, O. B., Bardeen, C. G., Mills, M. J., Fan, T., English, J. M., and Neely, R. R.: Evaluations of tropospheric aerosol properties simulated by the community earth system model with a sectional aerosol microphysics scheme, *Journal of Advances 1045 in Modeling Earth Systems*, 7, 865–914, <https://doi.org/10.1002/2014MS000421>, <http://doi.wiley.com/10.1002/2014MS000421>, 2015.
- Yu, H., Tan, Q., Zhou, L., Zhou, Y., Bian, H., Chin, M., Ryder, C. L., Levy, R. C., Pradhan, Y., Shi, Y., Song, Q., Zhang, Z., Colarco, P. R., Kim, D., Remer, L. A., Yuan, T., Mayol-Bracero, O., and Holben, B. N.: Observation and modeling of the 1050 historic “Godzilla” African dust intrusion into the Caribbean Basin and the southern US in June 2020, *Atmos. Chem. Phys.*, 21, 12359–12383, <https://doi.org/10.5194/acp-21-12359-2021>, 2021.
- Zhang, L., Montuoro, R., McKeen, S. A., Baker, B., Bhattacharjee, P. S., Grell, G. A., Henderson, J., Pan, L., Frost, G. J., McQueen, J., Saylor, R., Li, H., Ahmadov, R., Wang, J., Stajner, I., Kondragunta, S., Zhang, X., and Li, F.: Development and 1055 evaluation of the Aerosol Forecast Member in the National Center for Environment Prediction (NCEP)'s Global Ensemble Forecast System (GEFS-Aerosols v1), *Geosci. Model Dev.*, 15, 5337–5369, <https://doi.org/10.5194/gmd-15-5337-2022>, 2022.
- Zhong, Q., Schutgens, N., van der Werf, G.R., Bauer, S.E., Tsigaridis, K., Mielonen, T., Checa-Garcia, R., Neubauer, D., Kipling, Z., Kirkevag, A., Olivie., D.J.L., Kokkola, H., Matsui, H., Ginoux, P., Takemura, T., Le Sager, P., Remy, S., Bian, 1060 H., and Chin, M.: Using modelled relationships and satellite observations to attribute modelled aerosol biases over biomass burning regions, *Nat Commun*, 13, 5914, <https://doi.org/10.1038/s41467-022-33680-4>, 2022.

Figures

1065



1070 Figure 1: Emissions of (a) dust, sea salt, (b) black carbon, (c) organic carbon, (d) brown carbon, and (e) sulphate as well as the production of (d) brown carbon from secondary organic aerosol, (e) sulphate, and (f) nitrate averaged for the period of January 2016 through December 2019 in the GEOS GOCART-2G benchmark simulation.

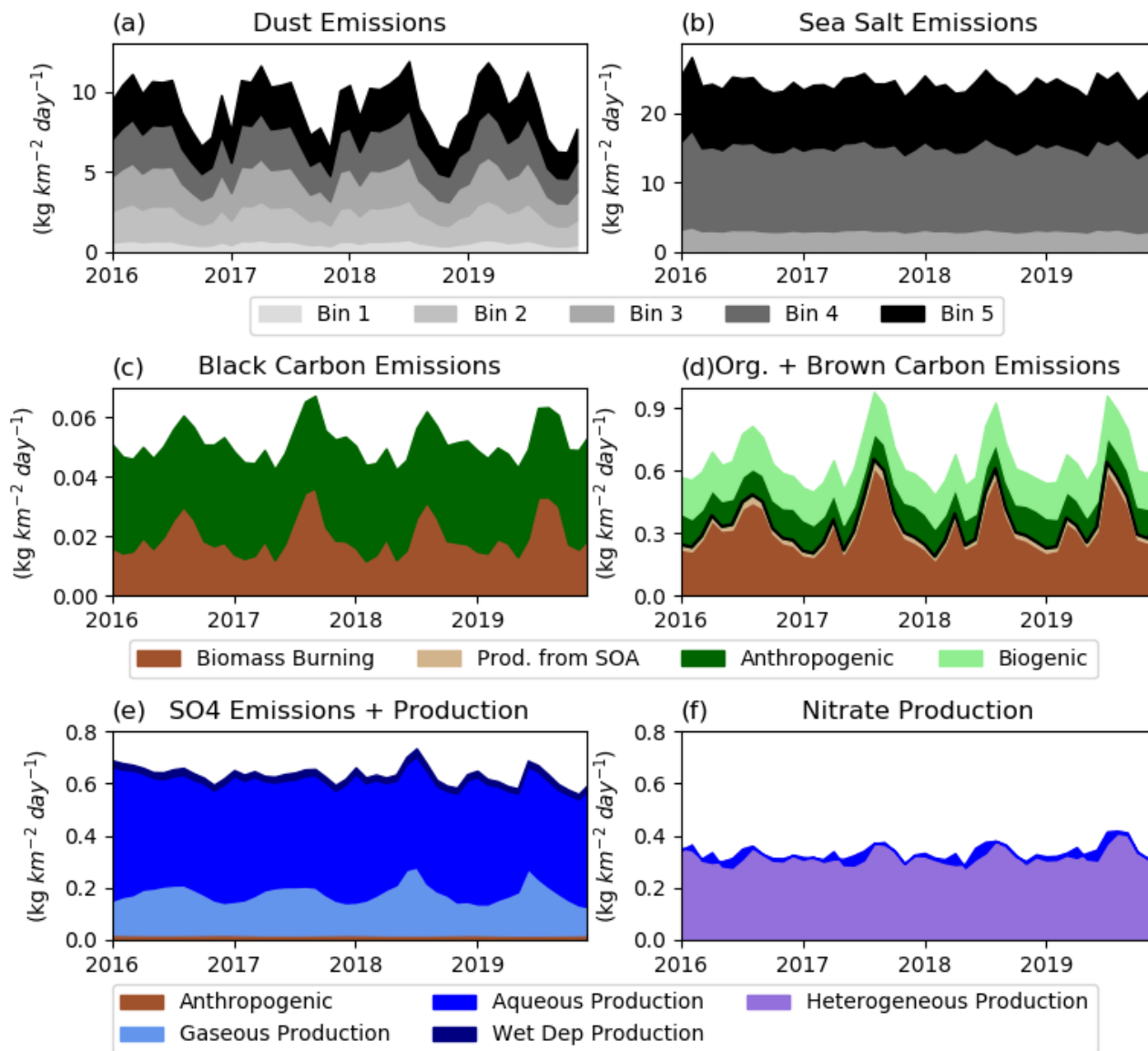
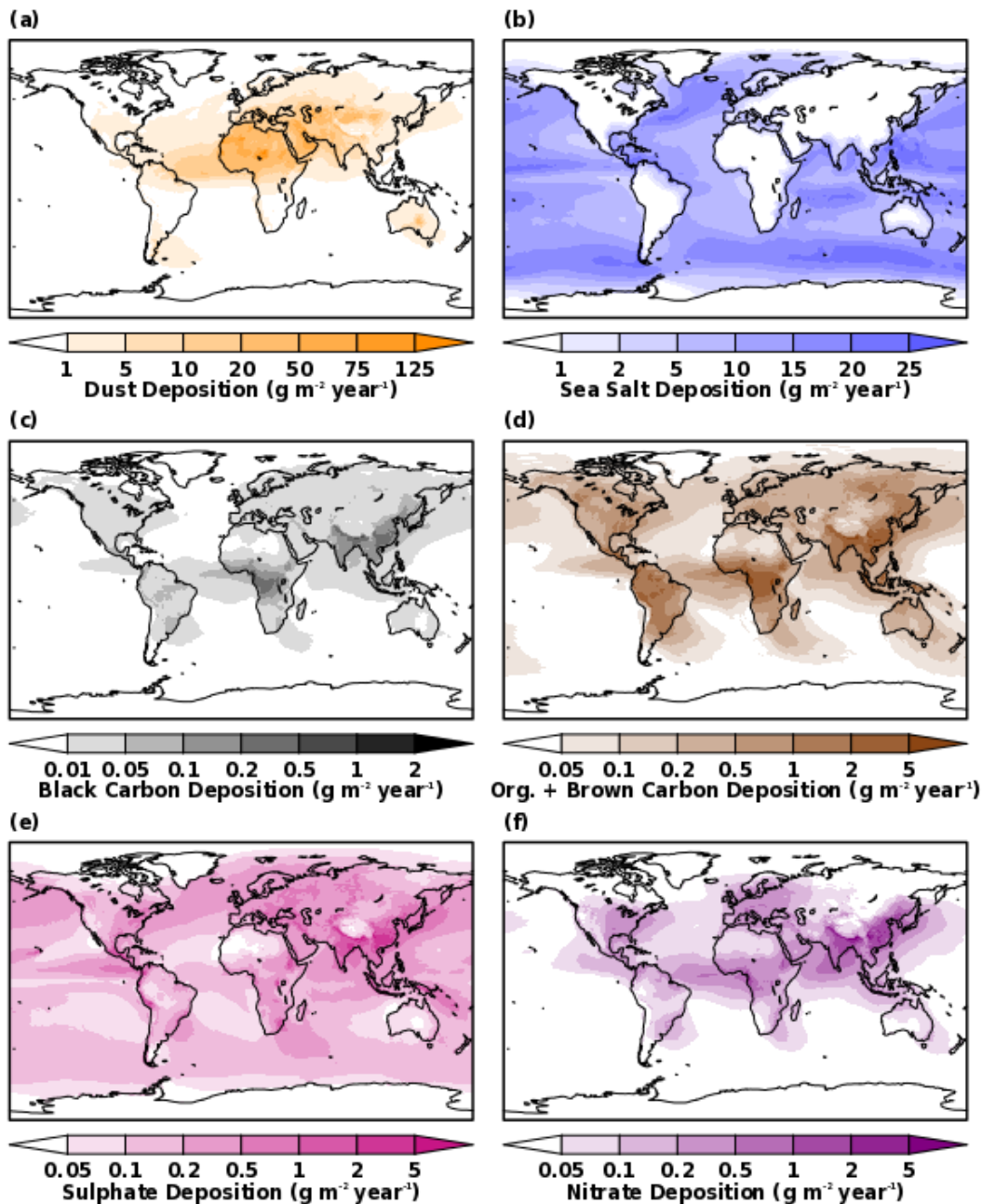
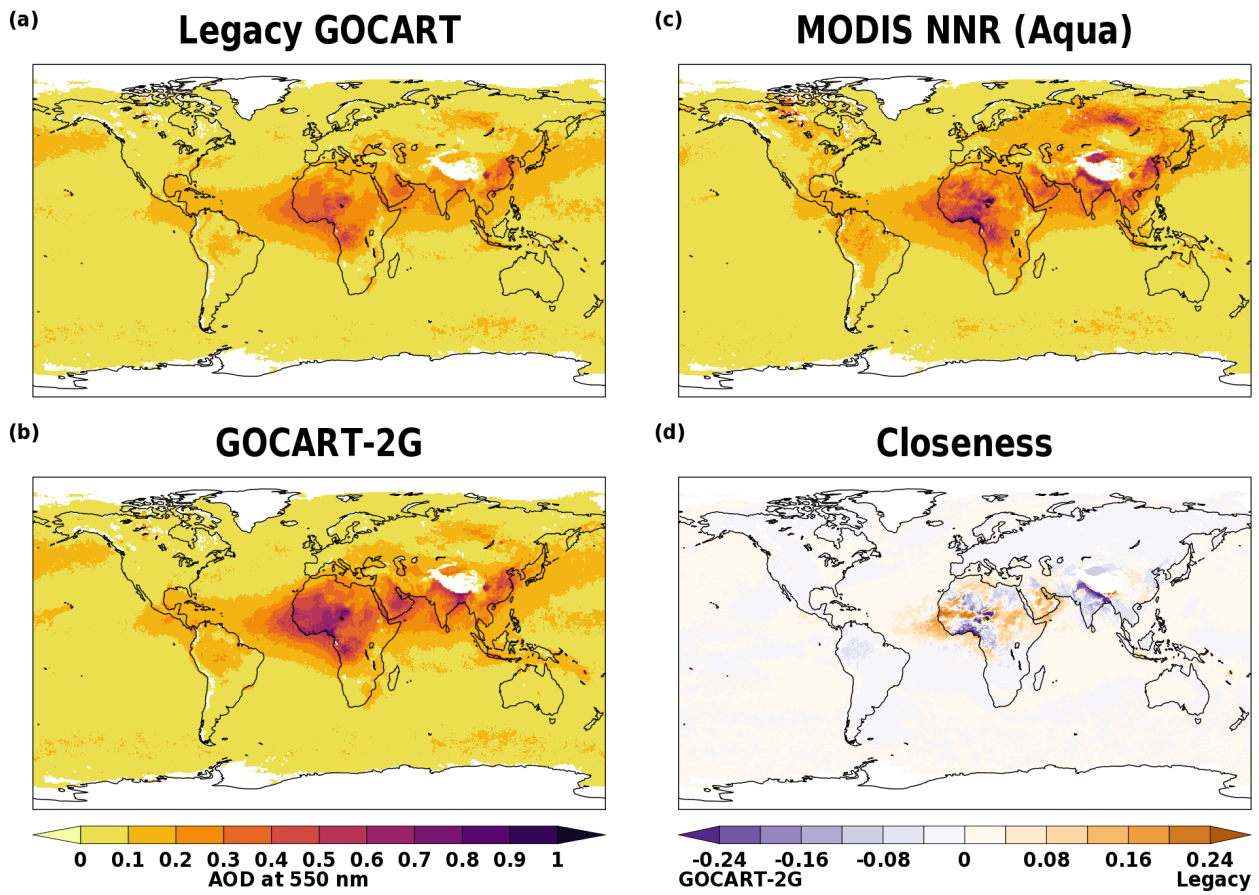


Figure 2: Timeseries of emissions and production of (a) dust, (b) sea salt, (c) black carbon, (d) organic carbon, brown carbon, (e) sulphate, and (f) nitrate for the period of January 2016 through December 2019 in the GEOS GOCART-2G benchmark simulation.

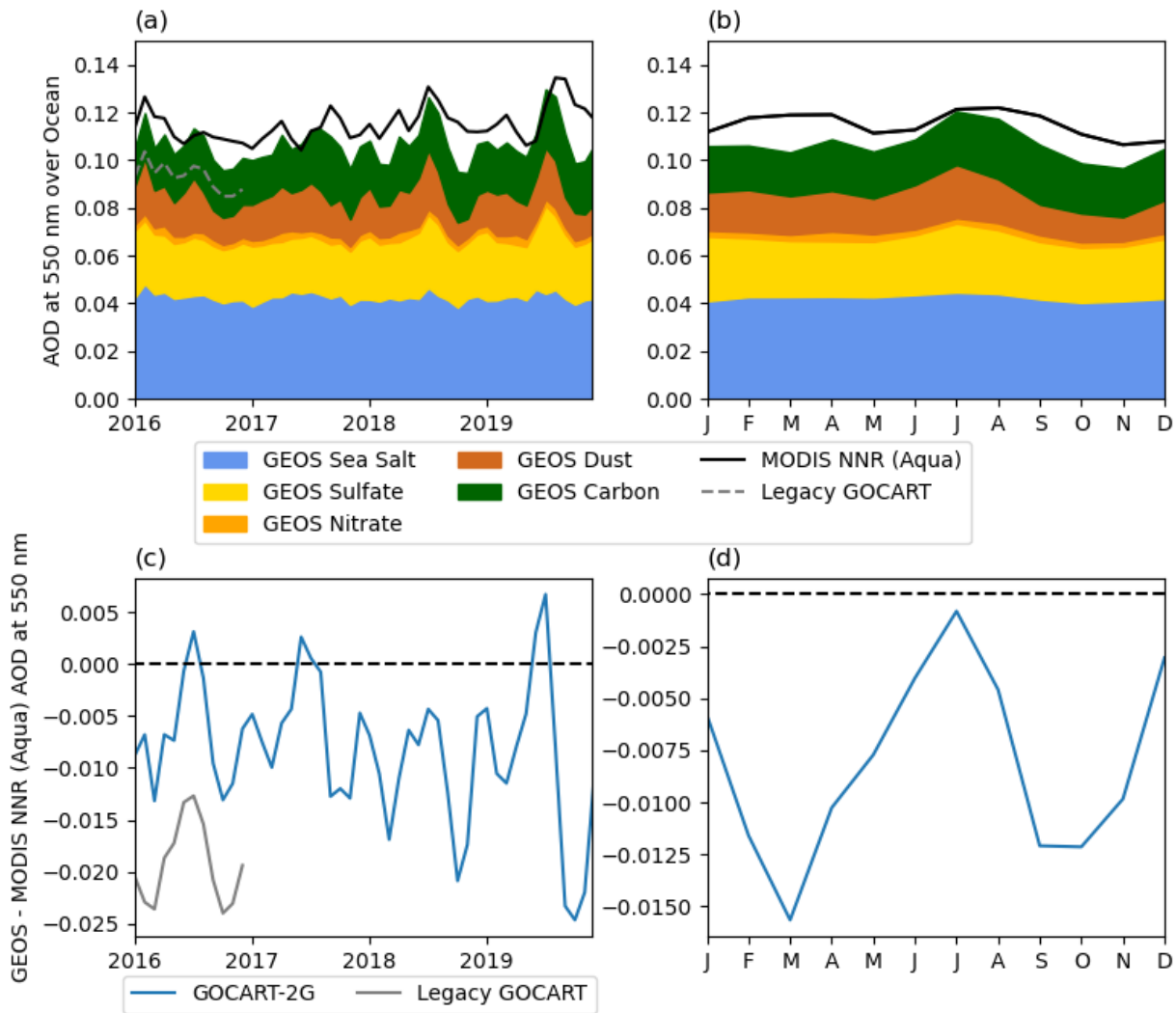


1075

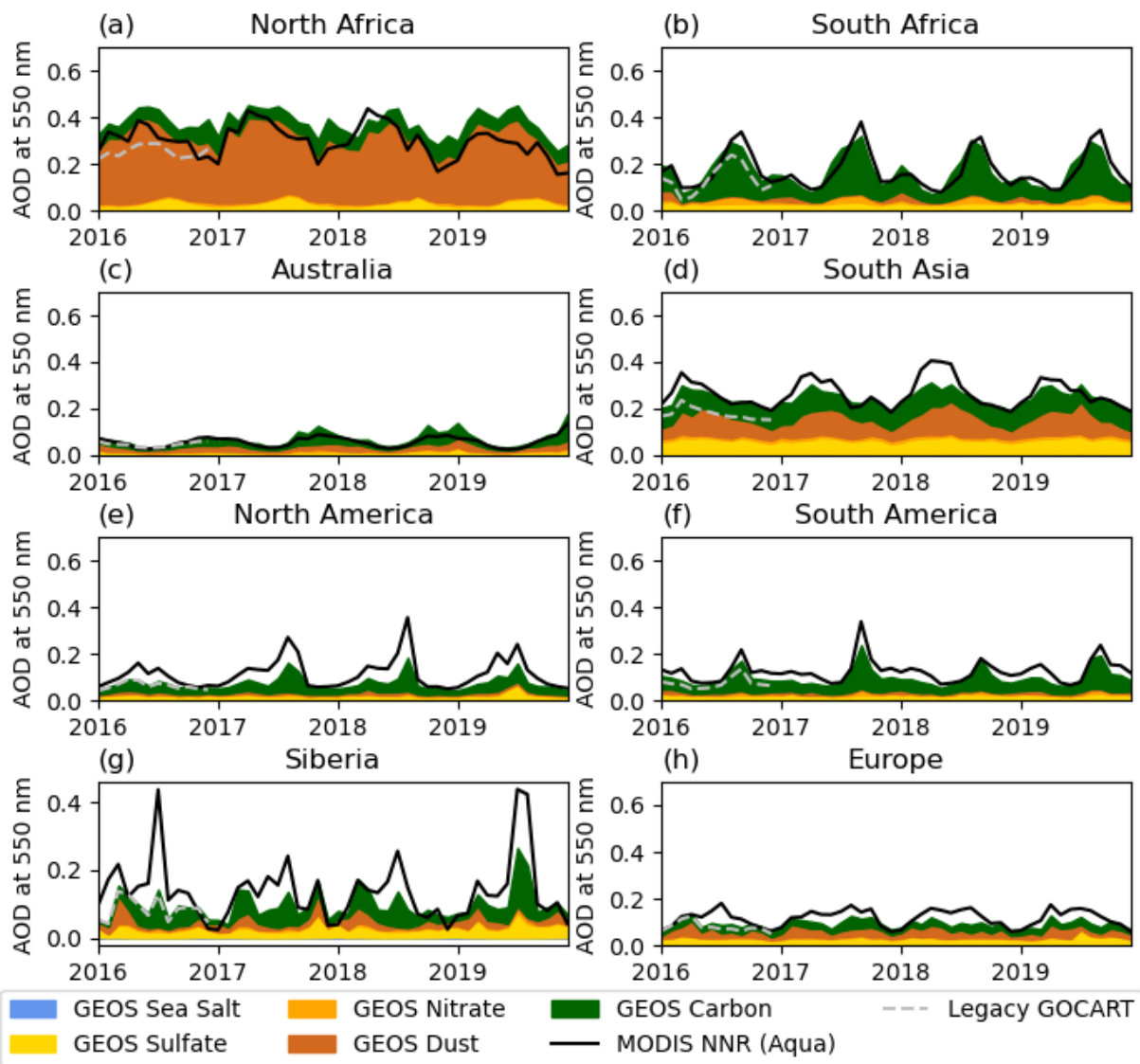
Figure 3: Deposition of (a) dust, sea salt, (b) black carbon, (c) organic carbon, (d) brown carbon, (e) sulphate, and (f) nitrate averaged for the period of January 2016 through December 2019 in the GEOS GOCART-2G benchmark simulation.



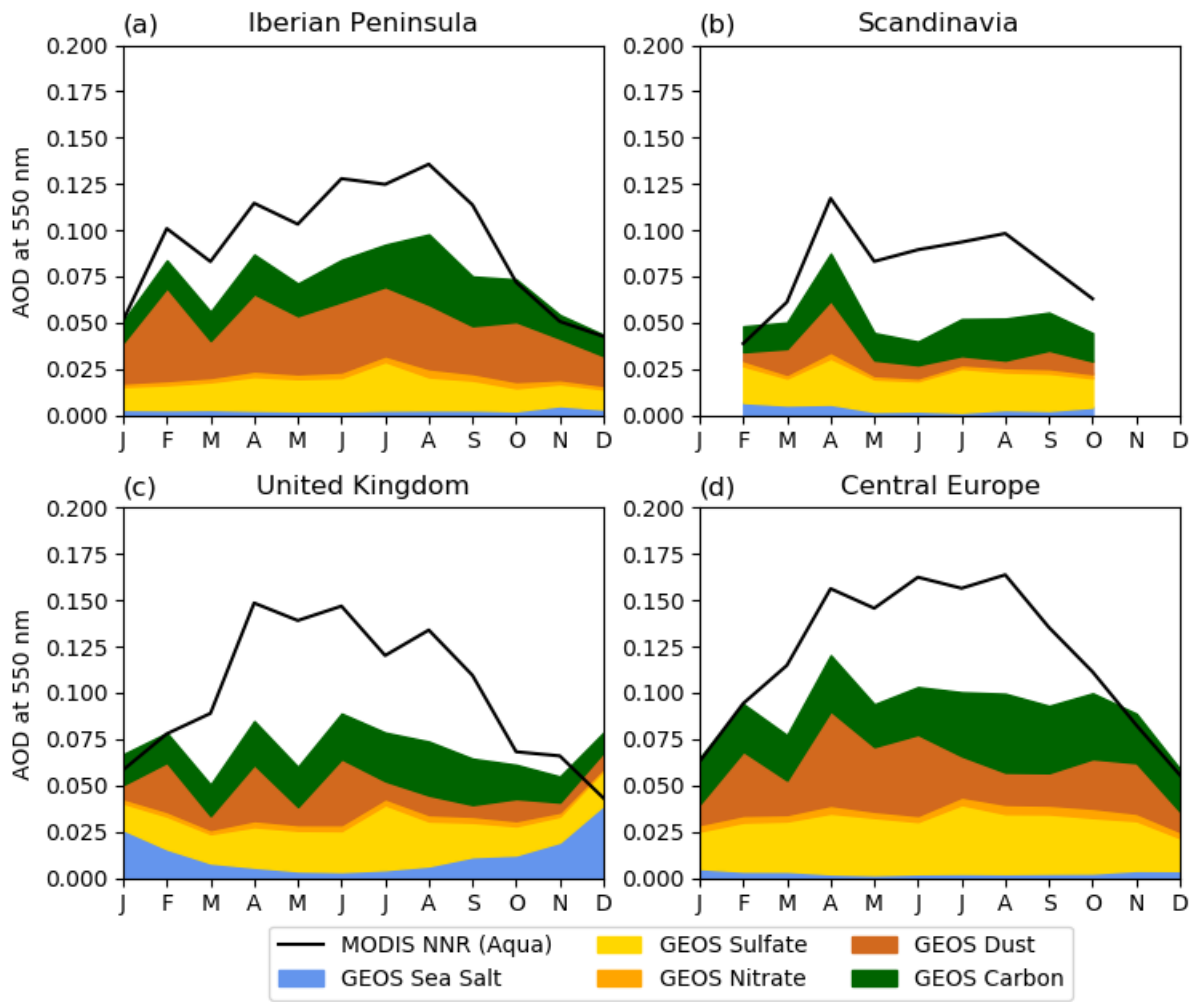
080 Figure 4: Average AOD at 550 for the period of January 2016 through December 2016⁹ in the (a) [GEOS Legacy GOCART simulation](#), (b) [GEOS GOCART-2G benchmark simulation](#), (c) [MODIS NNR observational product from Aqua](#), and (d) [the difference between the model and observations: closeness to the observations defined as \$|GOCART-2G-MODIS| - |Legacy GOCART-MODIS|\$](#) .



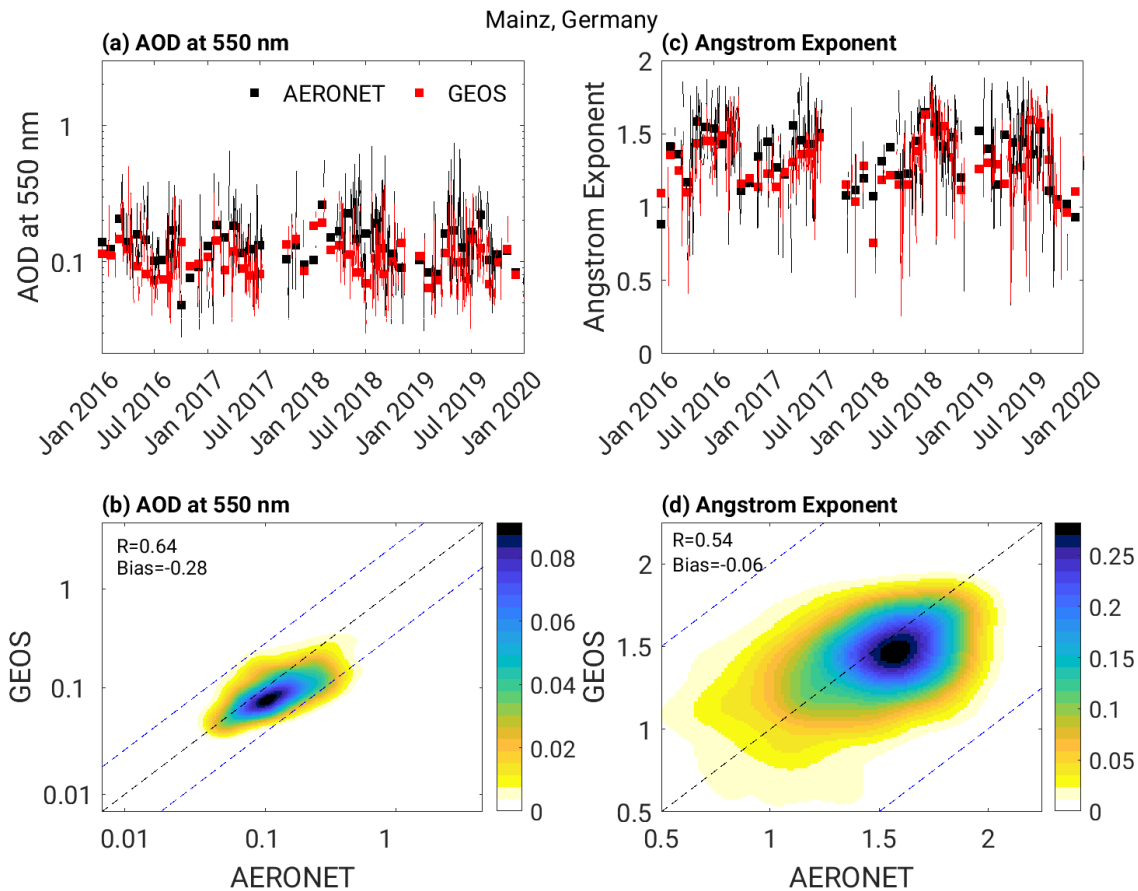
1085 **Figure 5: Timeseries of ocean area-averaged (a) monthly mean AOD from the Aqua MODIS NNR observational product and the speciated AOD from the GEOS GOCART-2G benchmark simulation, (b) mean seasonal cycle, and the difference between the model and observations for the (c) monthly mean AOD and (d) seasonal cycle of AOD. Total AOD in the Legacy GOCART simulation is added in grey lines for reference in (a) and (c).**



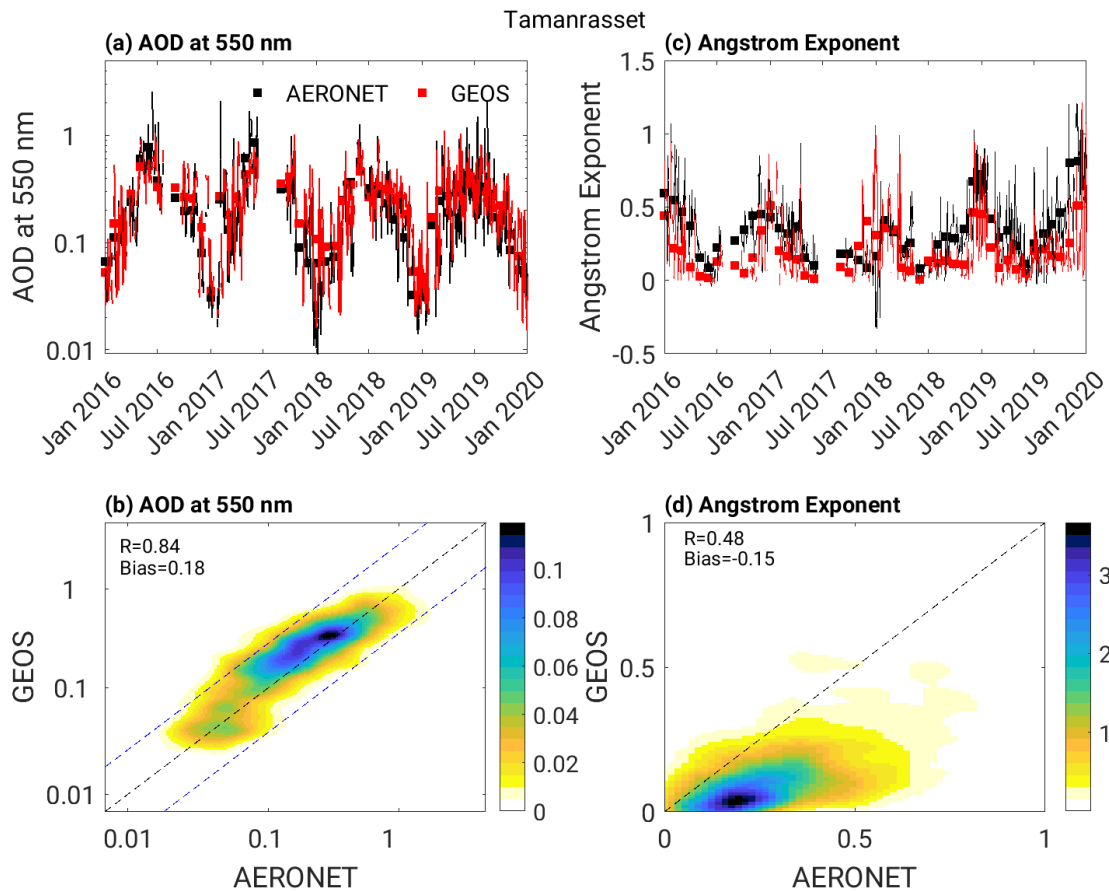
1090 **Figure 6: Timeseries of area-averaged monthly mean AOD from the Aqua MODIS NNR observational product and the speciated AOD from the GEOS GOCART-2G benchmark simulation over (a) North Africa, (b) South Africa, (c) Australia, (d) South Asia, (e) North America, (f) South America, (g) Siberia, and (h) Europe. Total AOD in the Legacy GOCART simulation is added in dashed grey lines for reference.**



1095 **Figure 7: Timeseries of area-averaged monthly mean AOD from the Aqua MODIS NNR observational product and the speciated AOD from the GEOS GOCART-2G benchmark simulation over (a) the Iberian Peninsula, (b) Scandinavia, (c) the United Kingdom, and (d) central Europe.**



1100 **Figure 8:** (a) Timeseries of hourly AOD at 550 nm, (b) 2-D kernel density estimate for AOD at 550 nm computed as $\log(\text{AOD}+0.01)$, (c) timeseries of Angstrom exponent, and (d) (e) 2-D kernel density estimate for Angstrom exponent over the AERONET station in Mainz, Germany for all co-located data points from the observations and GEOS GOCART-2G benchmark simulation. The statistics in (b) are computed as $\log(\text{AOD}+0.01)$. The black dashed line in (b) and (d) indicates the one-to-one line with the blue dashed lines are the one-to-one line plus or minus one of the one-to-one line.



1105 **Figure 9:** (a) Timeseries of hourly AOD at 550 nm, (b) 2-D kernel density estimate for AOD at 550 nm computed as $\log(\text{AOD}+0.01)$,
 (c) timeseries of Angstrom exponent, and (d) (e) 2-D kernel density estimate for Angstrom exponent over the AERONET station in
 Tamanrasset, Algeria for all co-located data points from the observations and GEOS GOCART-2G benchmark simulation. The
 statistics in (b) are computed as $\log(\text{AOD}+0.01)$. The black dashed line in (b) and (d) indicates the one-to-one line with the blue
 dashed lines are the one-to-one line plus or minus one of the one-to-one line.

1110

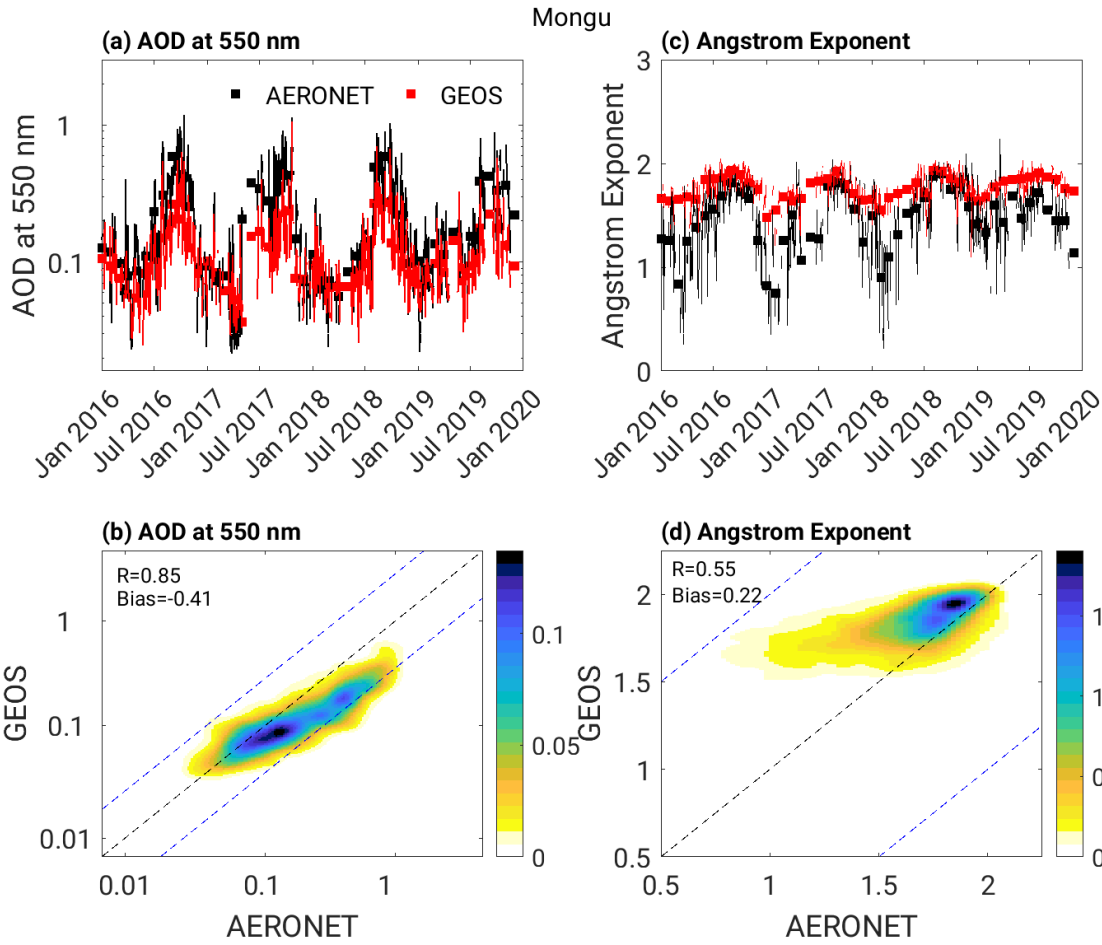
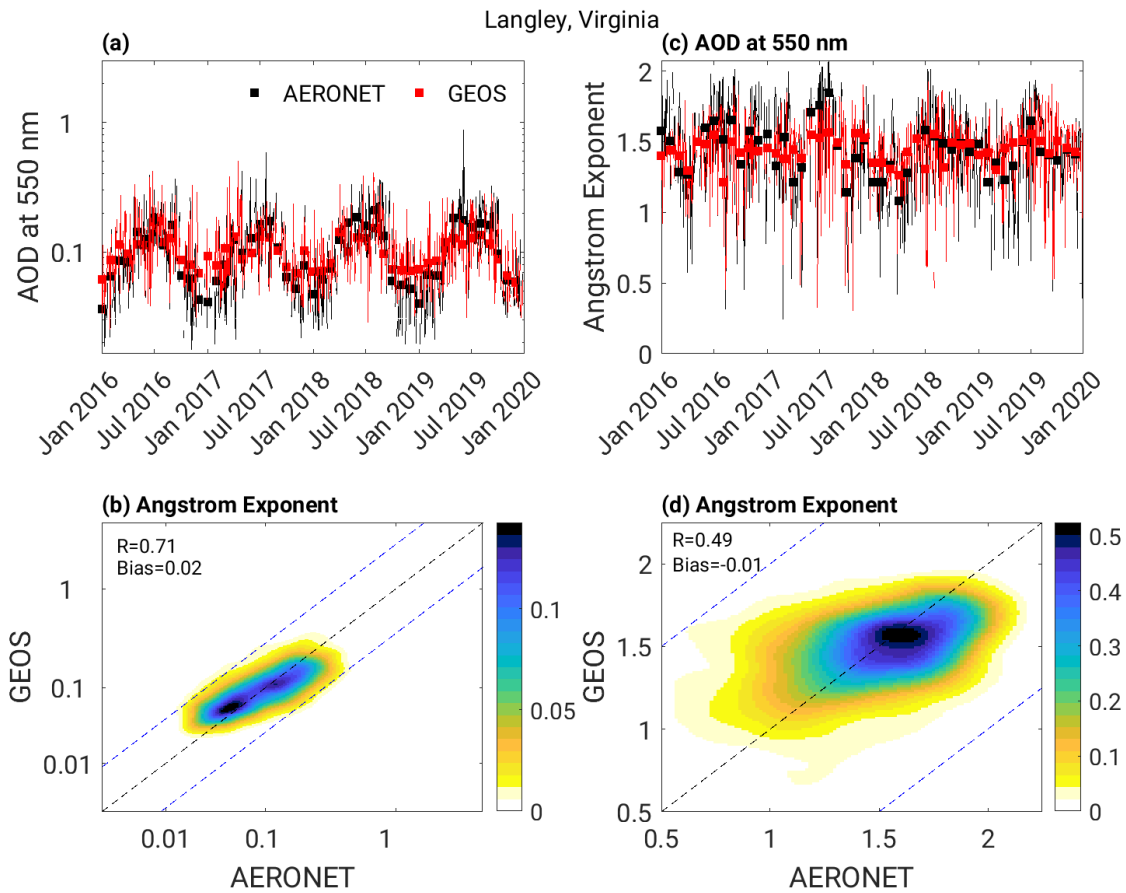
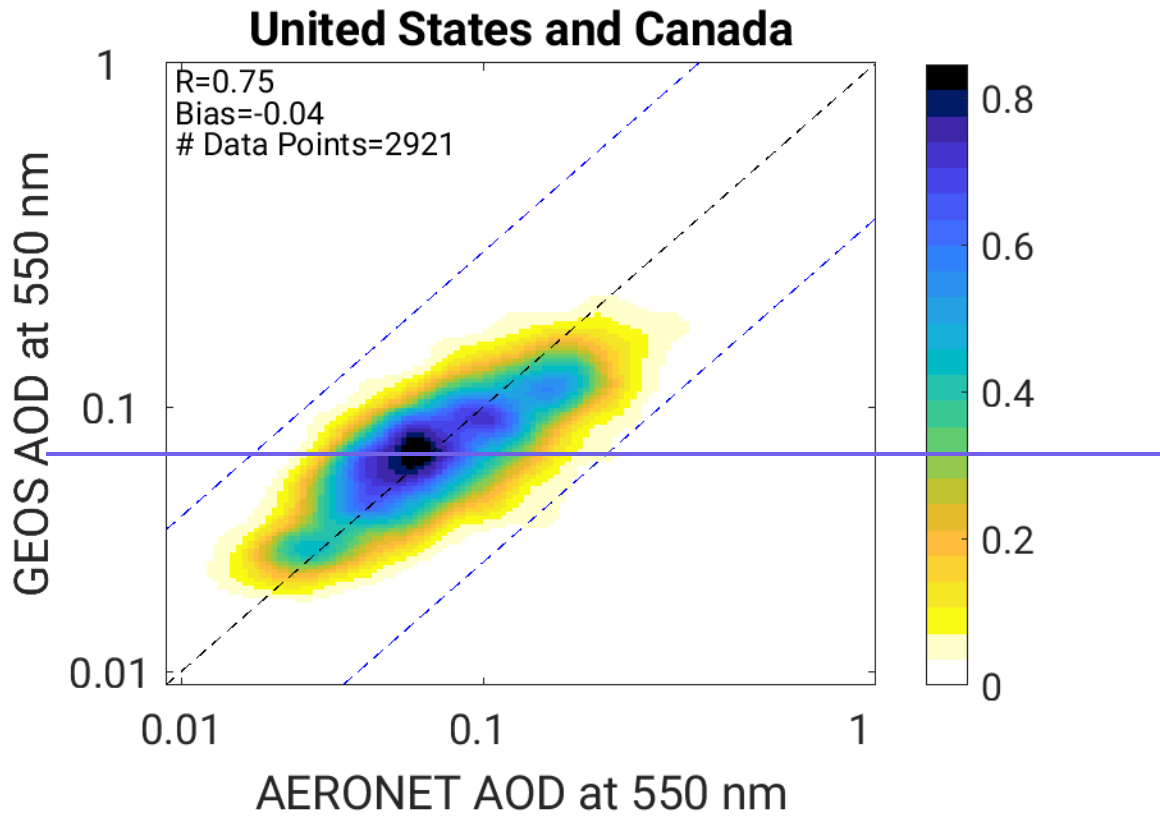


Figure 10: (a) Timeseries of hourly AOD at 550 nm, (b) 2-D kernel density estimate for AOD at 550 nm computed as $\log(\text{AOD}+0.01)$, (c) timeseries of Angstrom exponent, and (d) 2-D kernel density estimate for Angstrom exponent over the AERONET station in Mongu, Zambia for all co-located data points from the observations and GEOS GOCART-2G benchmark simulation. The statistics in (b) are computed as $\log(\text{AOD}+0.01)$. The black dashed line in (b) and (d) indicates the one-to-one line with the blue dashed lines are the one-to-one line plus or minus one of the one-to-one line.

115

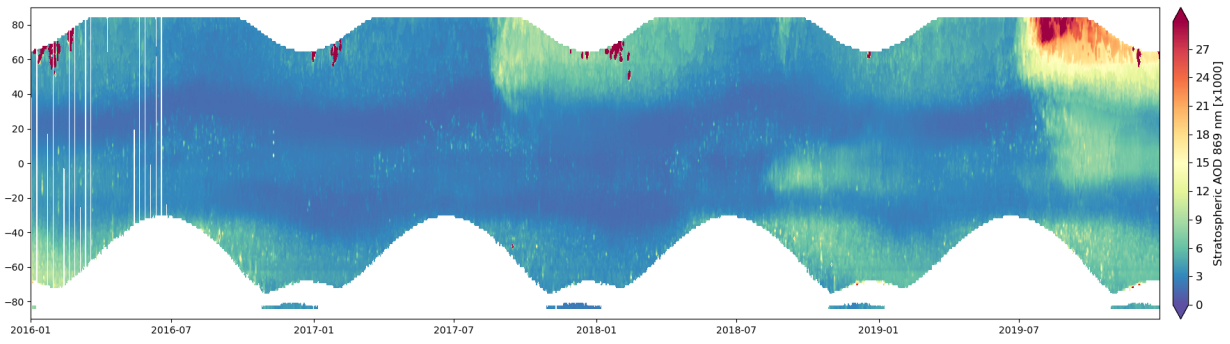


1120 **Figure 11: (a) Timeseries of hourly AOD at 550 nm, (b) 2-D kernel density estimate for AOD at 550 nm computed as $\log(\text{AOD}+0.01)$, (c) timeseries of Angstrom exponent, and (d) (e) 2-D kernel density estimate for Angstrom exponent over the AERONET station in Langley, Virginia for all co-located data points from the observations and GEOS GOCART-2G benchmark simulation. The statistics in (b) are computed as $\log(\text{AOD}+0.01)$. The black dashed line in (b) and (d) indicates the one-to-one line with the blue dashed lines are the one-to-one line plus or minus one of the one-to-one line.**

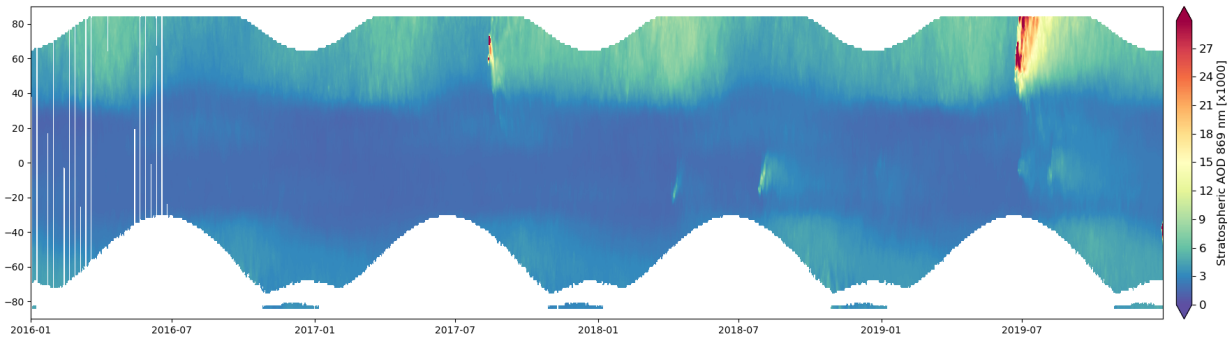


125 ~~Figure 12: 2-D kernel density estimate for AOD at 550 nm computed as $\log(\text{AOD}+0.01)$ from 77 AERONET stations across the United States and Canada for co-located data points from the observations and the GOCART 2G benchmark simulation. The statistics are computed as $\log(\text{AOD}+0.01)$. The black dashed line in (b) and (d) indicates the one-to-one line with the blue dashed lines are the one-to-one line plus or minus one of the one-to-one line.~~

1130 A.

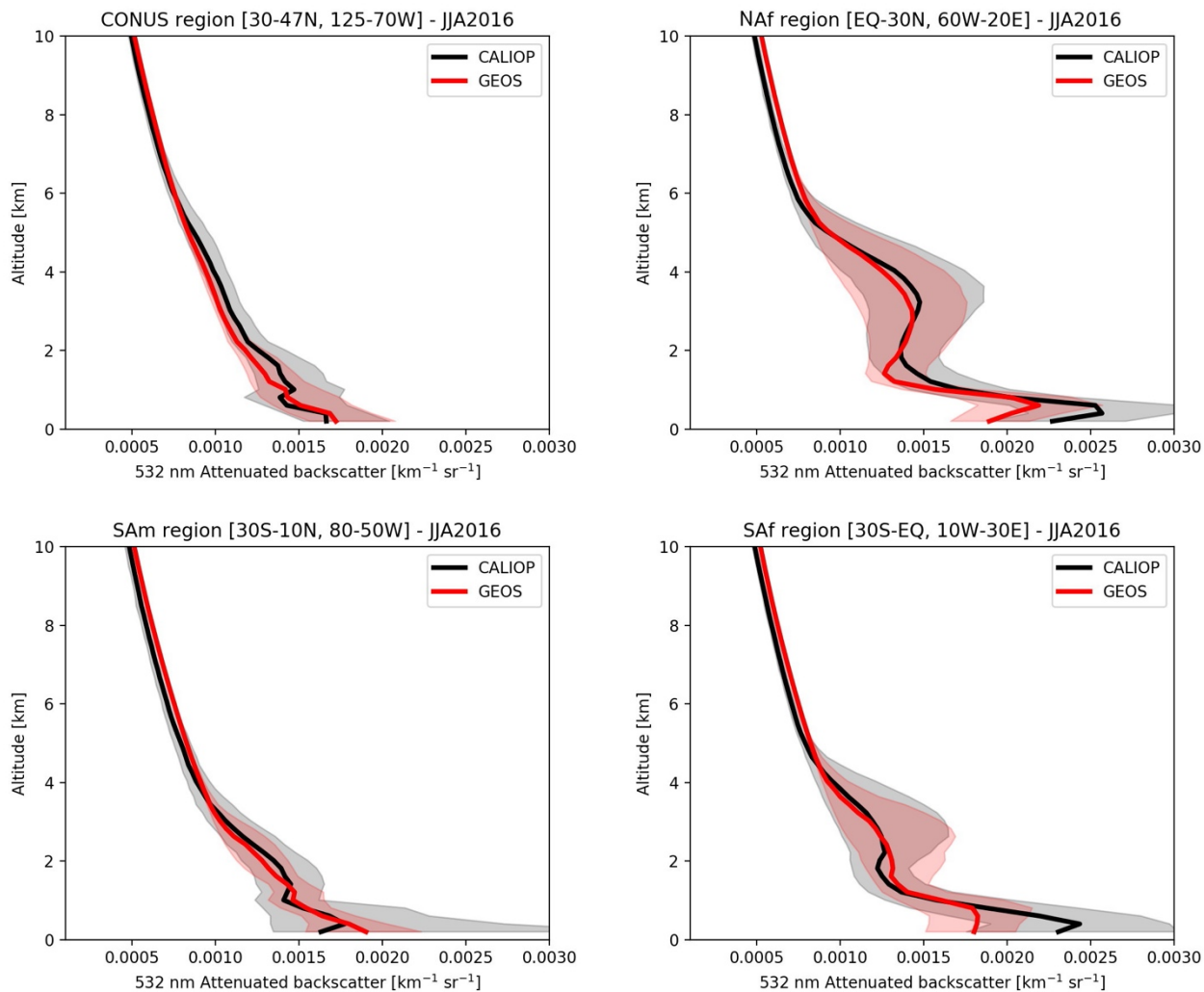


B.

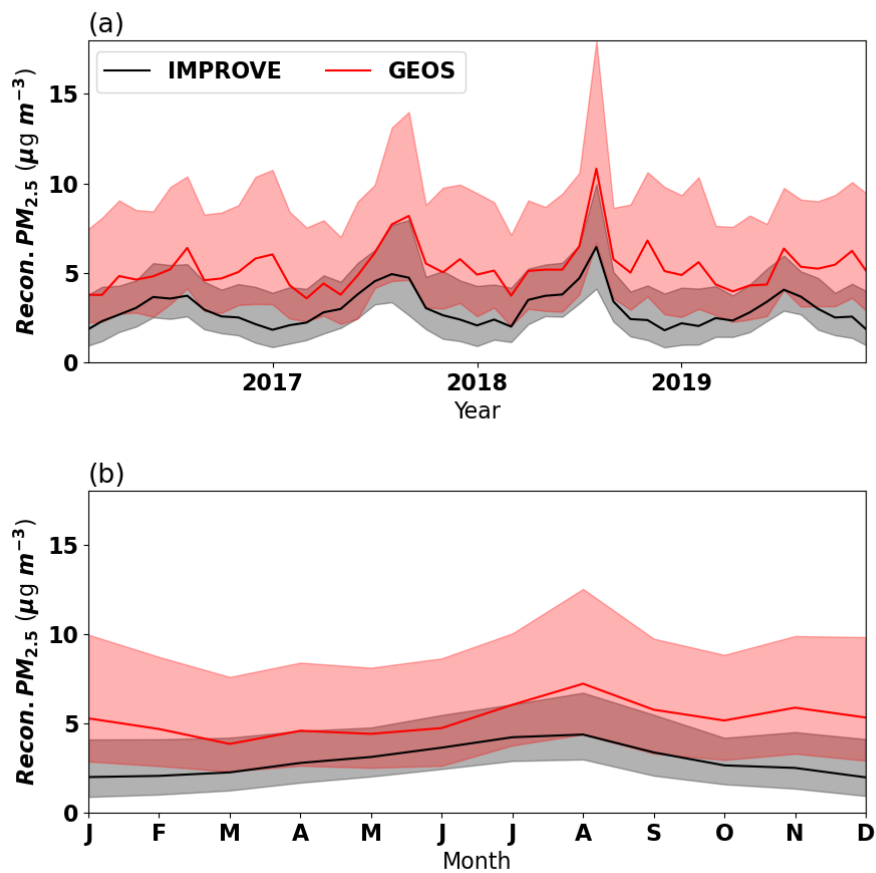


135 **Figure 4312:** Timeseries of zonal mean stratospheric AOD at 869 nm from (a) OMPS-LP observations and (b) the GEOS GOCART-2G benchmark simulation.

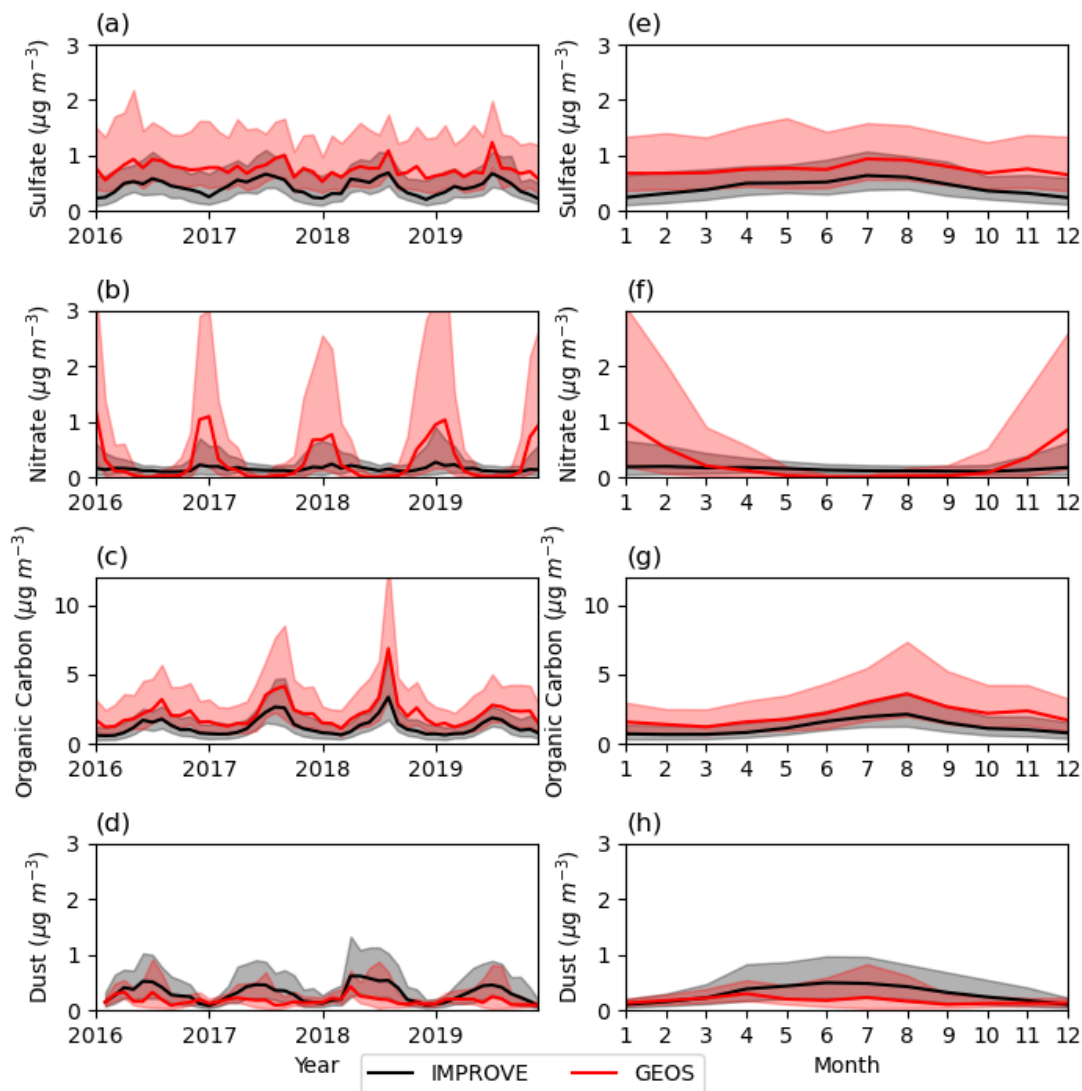
1140



145 | **Figure 1413:** Vertical profiles of total (aerosols + molecular) attenuated backscatter coefficient ($\text{km}^{-1} \text{sr}^{-1}$) at 532 nm and derived from GEOS GOCART-2G simulations sampled on the CALIOP path and averaged over the continental United States, northern Africa (top row), South America and southern Africa (bottom row) for the period of June-July-August 2016. The solid lines are the median of all profiles for CALIOP (black) and GEOS GOCART-2G (red). Shaded areas represent the 25th-75th percentile of all modelled and observed profiles.

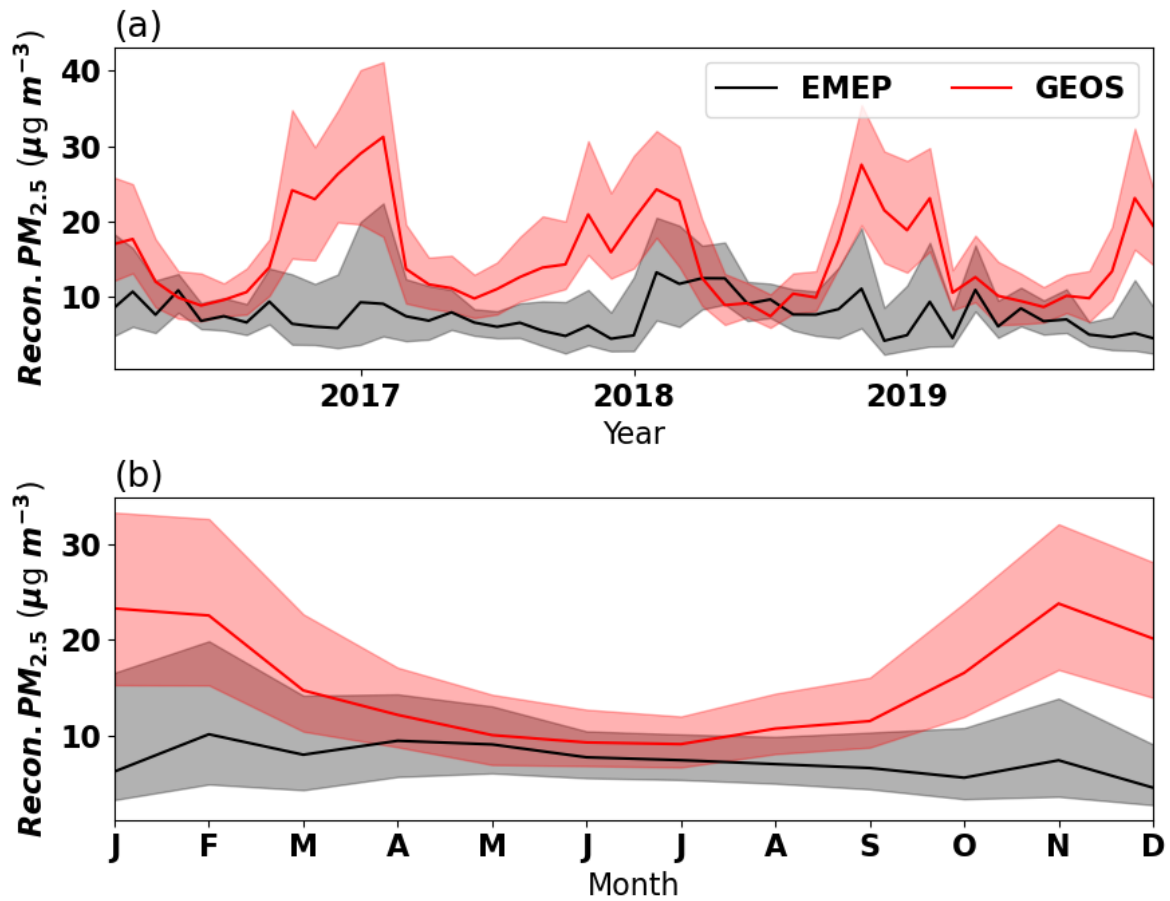


[150] Figure 1514: (a) Timeseries of monthly median and (b) median seasonal cycle of reconstructed $PM_{2.5}$ for the IMPROVE monitoring stations across the United States from the observations and GEOS GOCART-2G benchmark simulation. Shading lies between the 25th and 75th percentiles.

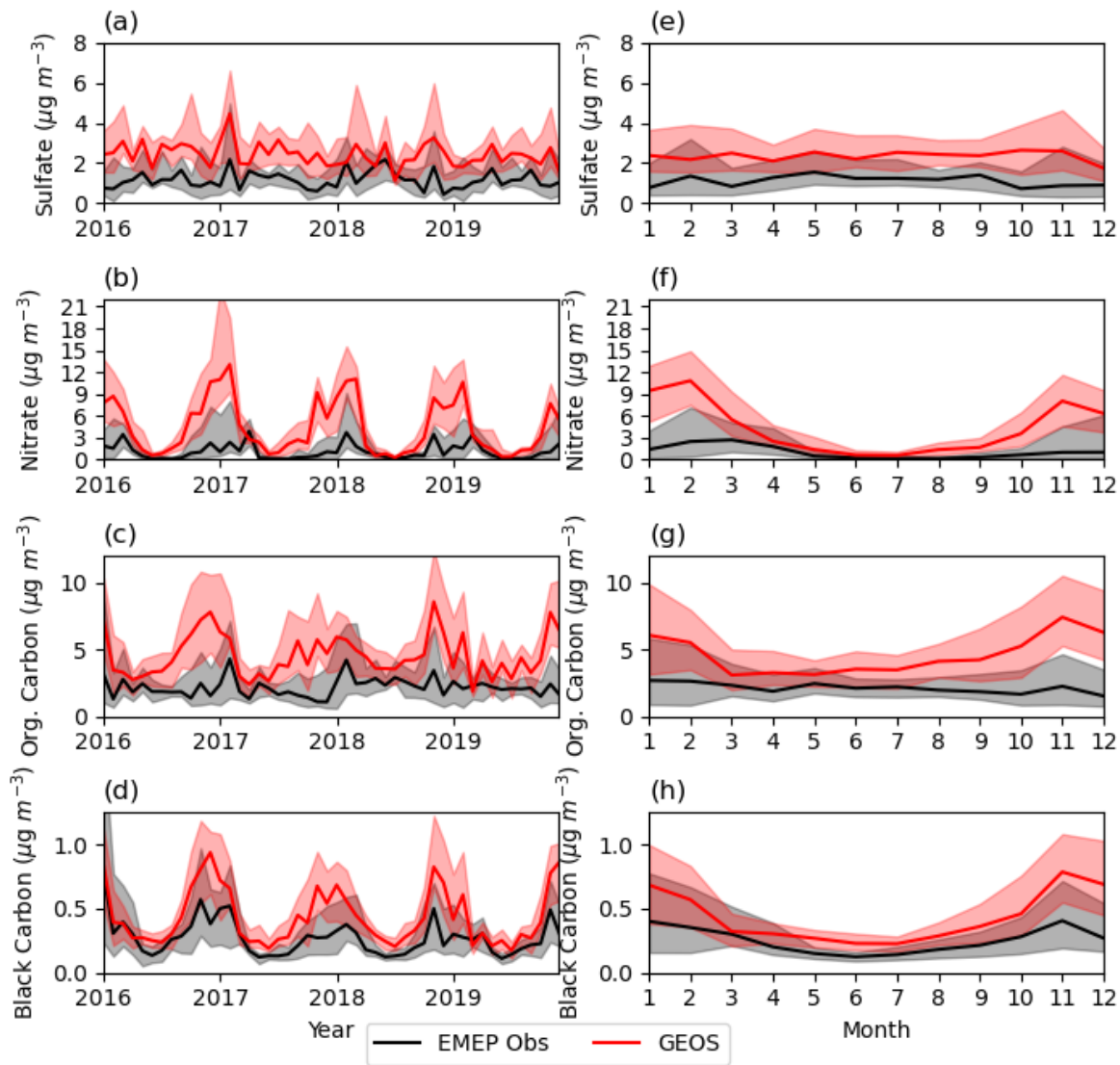


155

Figure 4615: Timeseries of the monthly median and median seasonal cycle for fine (a, e) sulphate, (b, f) nitrate, (c, g) organic carbon, and (d, h) dust averaged for the IMPROVE monitoring stations across the United States from the observations and GEOS GOCART-2G benchmark simulation. Shading lies between the 25th and 75th percentiles.



160 | Figure 4716: (a) Timeseries of monthly median and (b) median seasonal cycle of reconstructed $PM_{2.5}$ from four EMEP monitoring stations across Germany and one in Poland from the observations and GEOS GOCART-2G benchmark simulation. Shading lies between the 25th and 75th percentiles.



165 | **Figure 178:** Timeseries of the monthly median and median seasonal cycle for fine (a, e) sulphate, (b, f) nitrate, (c, g) organic carbon, and (d, h) black carbon for four EMEP stations across Germany and one in Poland from the observations and GEOS GOCART-2G benchmark simulation. Shading lies between the 25th and 75th percentiles.

Table A1. Aerosol particle size ranges for dust, sea salt, carbon, sulphate, and nitrate in GOCART-2G. Note a lower and upper radius is not given for carbon or sulphate as there are not discrete size bins.

Aerosol Bin	Effective Radius Assumed for Radiation (μm)	Radius Lower Bound (μm)	Radius Upper Bound (μm)
DU001	0.636	0.1	1
DU002	1.324	1	1.8
DU003	2.301	1.8	3
DU004	4.167	3	6
DU005	7.671	6	10
SS001	0.079	0.03	0.1
SS002	0.316	0.1	0.5
SS003	1.119	0.5	1.5
SS004	2.818	1.5	5
SS005	7.772	5	10
BC	0.0392		
BR	0.0876		
OC	0.0876		
SU	0.156		
NI001	0.156		
NI002	2.10		
NI003	6.86		

Table A2. Optics table versions in the initial release of GOCART-2G

Specie	Optics Table
Black Carbon	optics_BC.v1_3.nc
Brown Carbon	optics_BRC.v1_5.nc
Dust	optics_DU.v15_3.nc
Nitrate	optics_NI.v2_5.nc
Organic Carbon	optics_OC.v1_3.nc
Sea Salt	optics_SS.v3_3.nc
Sulphate	optics_SU.v1_3.nc